Springer Series in Materials Science 146

Gennady G. Gladush
Igor Smurov

Physics of Laser Materials Processing

Theory and Experiment

Springer

Springer Series in
MATERIALS SCIENCE 146

Springer Series in
MATERIALS SCIENCE

Editors: R. Hull C. Jagadish R.M. Osgood, Jr. J. Parisi Z. Wang

The Springer Series in Materials Science covers the complete spectrum of materials physics, including fundamental principles, physical properties, materials theory and design. Recognizing the increasing importance of materials science in future device technologies, the book titles in this series reflect the state-of-the-art in understanding and controlling the structure and properties of all important classes of materials.

Please view available titles in *Springer Series in Materials Science*
on series homepage http://www.springer.com/series/856

Gennady G. Gladush
Igor Smurov

Physics of Laser Materials Processing

Theory and Experiment

With 514 Figures

Springer

Gennady G. Gladush
Troitsk Institute for Innovation and Fusion Research
Pushovikh str., Vladenie 12, 142190 Troitsk, Moscow region, Russia

and

Institute on Laser and Information Technologies RAS
1 Svyatoozerskaya St., 140700 Shatura, Moscow Region, Russia
E-mail: gladush@triniti.ru

Igor Smurov
Ecole Normale Supérieure de St-Etienne, DIPI Laboratory
Rue Jean Parot 58, 42023 Saint-Etienne, France
E-mail: smurov@enise.fr

Series Editors:

Professor Robert Hull
University of Virginia
Dept. of Materials Science and Engineering
Thornton Hall
Charlottesville, VA 22903-2442, USA

Professor Jürgen Parisi
Universität Oldenburg, Fachbereich Physik
Abt. Energie- und Halbleiterforschung
Carl-von-Ossietzky-Straße 9–11
26129 Oldenburg, Germany

Professor Chennupati Jagadish
Australian National University
Research School of Physics and Engineering
J4-22, Carver Building
Canberra ACT 0200, Australia

Dr. Zhiming Wang
University of Arkansas
Department of Physics
835 W. Dicknson St.
Fayetteville, AR 72701, USA

Professor R. M. Osgood, Jr.
Microelectronics Science Laboratory
Department of Electrical Engineering
Columbia University
Seeley W. Mudd Building
New York, NY 10027, USA

Springer Series in Materials Science ISSN 0933-033X
ISBN 978-3-642-19242-5 e-ISBN 978-3-642-19831-1
DOI 10.1007/978-3-642-19831-1
Springer Heidelberg Dordrecht London New York

Library of Congress Control Number: 2011934865

© Springer-Verlag Berlin Heidelberg 2011

This work is subject to copyright. All rights are reserved, whether the whole or part of the material is concerned, specifically the rights of translation, reprinting, reuse of illustrations, recitation, broadcasting, reproduction on microfilm or in any other way, and storage in data banks. Duplication of this publication or parts thereof is permitted only under the provisions of the German Copyright Law of September 9, 1965, in its current version, and permission for use must always be obtained from Springer. Violations are liable to prosecution under the German Copyright Law.

The use of general descriptive names, registered names, trademarks, etc. in this publication does not imply, even in the absence of a specific statement, that such names are exempt from the relevant protective laws and regulations and therefore free for general use.

Cover design: eStudio Calamar Steinen

Printed on acid-free paper

Springer is part of Springer Science+Business Media (www.springer.com)

Preface

We are glad to propose a new book *Laser Processing of Materials: Theory, Experiment* which combines theories and physical insights of industrial applications of lasers.

Despite the fact that interaction of laser beams with materials has been the subject of numerous books aimed to generalize the scientific backgrounds and techniques of laser processing some issues still remain unsolved. They build a long list of urgent tasks for communities of researchers and engineers around the globe. Many successful technological processes are known to have been developed empirically without a deep understanding of the triggering mechanisms and, moreover, lacking whatever quantitative theoretical or numeric description. Not all of the experimental regularities and phenomena are explained by theories. For example, in laser welding the origin of some weld defects is still open to question. The loss of efficiency at low welding speed in comparison with the electron-beam technique and generation of asperities on the weld surface at high speed is not currently understood. For the gas jet assisted cutting, there is a problem of the cut edge roughness. Selective laser sintering is known to be troubled by the quality losses, i.e. formation of droplets and at both slow and fast scanning speeds. This list can be continued to become a very long one.

Many resent books pay considerable attention to design and operation of laser systems, experimental setups and purely technological aspects. However, the presentation of the theories and simulations or any sort of mathematics is left rather fragmentary. For example, this can be very well seen in the excellent book by W. Steen, *Laser Material Processing*, Springer 2003. The fresh monograph by N.B. Dahotre, S.P. Harimkar, *Laser Fabrication and Machining of Materials*, Springer 2008, includes a lot of technical details of laser tools as auxiliaries to conventional methods of machining such as turning, grinding, drilling laser processing of equipment, manufacturing of three-dimensional objects with lasers, review of lasers in medicine and surgery. The introduction and review of theoretical models describing laser welding and cutting are brief and serve rather illustrative purposes. For a more detailed discussion of the mechanisms making the laser processing, one needs to see the book by E. Toyserkany, A. Khajepour, S. Corbin,

Laser Cladding, CRC press 2005. However, this book is devoted to the cladding techniques only. A lot of attention there is paid to the metallurgical processes which are studied in most cases empirically.

The book we present is intended to describe primarily the very mechanisms which make the basis of the laser processing techniques. A lot of attention is focused on the quantitative description. Here, using the similar vision angle, we aim to generalize the results including some new research directions. This should guide the reader through the diversity of parameters and help him determine the optimal processing modes.

The complexity of technological and physical processes is described using a unitary approach. We study a broad range of parameters which contribute to the nonresonant interaction of laser light with materials. These include pulse duration – from nanoseconds to the continuous wave mode, of the pulsed laser – from several units to hundreds, power density – from 10^4 to 10^{12} W/cm^2, beam power – from dozens of W to dozens of kW.

To make the book complete and self-consistent for every issue covered we are unwinding our description from elementary approaches to modern sophisticated models. The preference is granted to the models which have been verified in experiments. At the same time, we discuss important experimental results which have not yet obtained quantitative explanations as well as refer to theoretical models still waiting for their experimental verification.

Consequently, our book puts the stress on building the understanding of the cause-and-effect relations in physical processes employed in laser technologies. We expect it to become a useful supplement to the books published earlier. We hope it will help the engineers and researchers to improve the existing and develop new machining techniques. The book may serve as a textbook for under- and post-graduate students majoring in laser applications.

Acknowledgements

This book was made possible by the efforts of many people who offered their support and expertise. Without their encouragement, guidance, and sincere concern, many things would be different.

Our gratitude will go to all our colleagues and friends for fruitful discussions who have contributed their ideas, time, and energy, and especially to A. Gusarov, I. Yadroitsev, M. Doubenskaya, V. Mazhukin, W. Scharff, N. Rodionov, A. Krasyukov, S. Drobyazko, and Mrs. G. Antonova.

G. Gladush extends his heartily thanks to the staff of the Diagnostics and Engineering of Industrial Processes Laboratory (DIPI) of the National Engineering School of Saint-Etienne (ENISE) for the nice and friendly atmosphere during his staying with them, and especially to Mrs. I. Movchan for management and technical support.

G. Gladush also offers his profound thanks to M. Sapozhnikov, a valued specialist in English language for the precious time he gave up to go over the manuscript. To these acknowledgments must be added his deep gratitude to Mrs. E. Isaeva for the help in preparing figures.

G. Gladush takes this opportunity to express his profound gratitude to his beloved wife Galina and sons Maxim and Yuri. Without their support, cooperation, and preparation of the manuscript in LaTeX this book would not exist.

Finally, the authors thank all individuals who so graciously volunteered to dedicate their services, time, and support to our work.

Saint Etienne, Troitsk, Shatura — *Gennadiy Gladush*
March 2011 — *Igor Smurov*

Contents

Acronyms

c_p	Specific heat
d	Size
E	Pulse energy
F	Focal distance
H_b	Boiling heat
H_m	Melting heat
L_b	Length
L_m	Enthalpy at boiling temperature
L	Enthalpy at melting temperature
l	Optical thickness
l_R	Rosseland's path
m	Atom mass
M	Mach number
Ma	Marangoni number
n	Refractive index
P	Power
Pr	Prandtl number
Pe	Peclet number
Q	Heat or off-duty ratio (in Chaps. 8 and 9)
q_t	Thermal radiation flux
q_{tr}	Transmitted laser intensity
R	Reflection coefficient
Re	Reynolds number
r_f	Radius of focal spot
S	Surface
T	Temperature
Tr	Transmission coefficient
T_s	Surface temperature
t	Time
V	Velocity

S	Surface
α	Absorption coefficient of surface
α_H	Absorption coefficient of H_{01} mode
α_E	Absorption coefficient of E mode
δ	Fresnel number
ε	Permittivity in Chap. 1 and fraction of pores in Chap. 2
ε''	Imaginary part of permittivity
η	Dynamic viscosity
θ	Angle
κ	Thermal conductivity
λ	Wavelength
μ_a	Absorption coefficient
μ_s	Scattering coefficient
ν	Kinematic viscosity
ξ	Surface impedance
Π	Hertz potential
ρ	Density of material or specific resistance in Chap. 1
σ	Stephan–Boltzmann constant in Chap. 9, surface tension in Chap. 2, and electric conductivity in Chap. 1
τ	Pulse duration
χ	Thermal diffusivity
ψ	Wave phase
ω	Wave frequency

Chapter 1
General Problems of Propagation of Laser Radiation in Gases and Plasma and Physical Processes on the Surface of Condensed Media

Abstract Laser processing of materials is usually performed by focused radiation, many operations requiring very tight focusing. The focal spot size cannot be made as small as one likes due to diffraction of a light beam. The laser beam focusing can be also restricted by nonlinear processes. Because laser radiation used for material processing has high average or peak powers, this radiation can change the optical properties of media in which it propagates. The so-called self-action effects such as radiation self-focusing or self-defocusing appear. In addition, light can be noticeably absorbed in a medium. Technical industrial conditions may require sometimes the transport of light over long distances in air or through condensed media (in the case of special technologies), and these effects can become significant. Plasma often produced during various technological processes can strongly affect the propagation of light, in particular, IR radiation at $\lambda = 10\,\mu\mathrm{m}$. In this chapter, we consider this question only briefly. The propagation of radiation in the optical discharge plasma will be discussed in detail in Chap. 3. The efficiency of action of light incident on a sample depends on the absorption coefficient of the latter. For example, during laser welding and drilling light propagates in a narrow channel, where it is multiply reflected from walls. The properties of such propagation of light will be also considered in this chapter. Laser radiation can heat, melt, evaporate, and ionize the sample material. During heating in an oxidizing medium, the sample material can be oxidized. During melting of the sample, the motion of the melt can appear due to Marangoni effect and capillary instabilities can develop. If the radiation intensity is sufficient to initiate the evaporation of the target, specific evaporative instabilities can appear. We will briefly discuss all these phenomena in this chapter.

G.G. Gladush and I. Smurov, *Physics of Laser Materials Processing*,
Springer Series in Materials Science 146, DOI 10.1007/978-3-642-19831-1_1,
© Springer-Verlag Berlin Heidelberg 2011

1.1 Propagation and Focusing of Radiation in Vacuum, Gases and Plasma

1.1.1 Focusing of Light in Vacuum

As mentioned above, the tight focusing of light in vacuum is mainly prevented by diffraction. This phenomenon can be most simply described in the so-called quasi-wave approximation. The aim of this section is, in particular, the demonstration of the efficiency of this approximation. This is achieved by obtaining the known results on light focusing in vacuum. In this approximation, a wave remains quasi-monochromatic, and only its amplitude and phase change. Consider this approximation taking self-action into account [1]. The results will be used in the next sections.

Consider the propagation of a modulated wave in a medium with the permittivity depending on the wave intensity:

$$\varepsilon = \varepsilon_0 + \varepsilon_{\mathrm{nl}} \tag{1.1}$$

where ε_0 is the linear permittivity (the limiting value of ε for ($|E| \to 0$)) and $\varepsilon_{\mathrm{nl}}$ is the nonlinear addition. If $\varepsilon_{\mathrm{nl}}$ depends directly on the field strength, it can be represented as a series

$$\varepsilon_{\mathrm{nl}} = \varepsilon_2 |E|^2 + \varepsilon_4 |E|^4 + \ldots, \tag{1.2}$$

where the first term of the expansion corresponds to the polarization of the medium cubic in the field strength, and $\varepsilon_4 |E|^4$ corresponds to fifth-order polarization over the field, etc. The value of $\varepsilon_{\mathrm{nl}}$ can depend on the field strength not directly but via a different quantity depending on the field strength. Then, the equation for the field should be supplemented by the equation describing the dependence of this quantity on the field. The nonlinear change in the permittivity produces self-action effects. The wave still remains quasi-monochromatic during self-action, the nonlinear effect being manifested in variations in the amplitude and phase modulation of the wave and changes in the shape of its angular distribution and frequency spectrum.

The stationary self-action of waves in a medium with permittivity (1.1) is described by the Helmholtz equation

$$\Delta E = \frac{\omega^2}{c^2} \varepsilon_0 E + \frac{\omega^2}{c^2} \varepsilon_{\mathrm{nl}} E \tag{1.3}$$

where ω is the frequency of light and E is the electric field strength vector of the wave.

In the case of the wave beams with a narrow angular distribution and the weak nonlinearity of the medium, the solution of the latter equation can be simplified by using the method of slowly varying amplitudes.

Lets us represent the wave field of a diffracting beam in the form of a quasi-plane wave

$$E = (e/2)E(\mu z, \sqrt{\mu}x, \sqrt{\mu}y)\exp[\mathrm{i}(\omega t - kz)] + c.c. \tag{1.4}$$

where e is the unit polarization vector; z is the beam propagation direction; x and y are the transverse coordinates; E is the slowly varying amplitude; μ is a small parameter characterizing the difference of the beam from a linear plane wave, which is manifested due to diffraction and the nonlinearity of the medium; and k is the wave-vector modulus. Expression (1.4) takes into account that variations in the complex amplitude across the wave beam occur faster than along the beam. By assuming that the nonlinearity of the medium has the same order of smallness, $\mu_1\varepsilon_{\mathrm{nl}} \sim \mu\varepsilon_0$, and substituting (1.4) into (1.3), we obtain in the first approximation in a small parameter the equation

$$2\mathrm{i}k\frac{\partial E}{\partial z} = \Delta_\perp E + k^2\frac{\varepsilon_{\mathrm{nl}}}{\varepsilon_0}E, \quad E = E_0(r,z)\exp[\mathrm{i}k\psi(r,z)] \tag{1.5}$$

where ψ is the phase.

Equation (1.5) corresponds to the quasi-optical approximation in the theory of nonlinear waves. It describes the stationary self-action of diffracting wave beams. The linear and nonlinear parts of the permittivity entering (1.5) are complex functions: $\varepsilon \approx \varepsilon' + \mathrm{i}\varepsilon''$.

If the linear and nonlinear absorption of the wave is small, ε and $\varepsilon_{\mathrm{nl}}$ are real quantities. Then, the term with $\varepsilon_{\mathrm{nl}}$ in parabolic equation (1.5) describes the dependence of the phase velocity on intensity.

Note that (1.5) in vacuum is transformed to a linear parabolic equation with the imaginary diffusion coefficient $D_k = -1/2\mathrm{i}k$. The diffusion equation has the general solution expressing the required function in terms of its boundary value. This solution shows that, if the beam has a Gaussian distribution on a focusing spherical mirror, this distribution is preserved during the propagation of the beam in vacuum:

$$E_0 = \frac{E(0)}{\sqrt{(1-z/F)^2 + D^2}}\exp\left\{-\frac{r^2}{a^2[(1-z/F)^2 + D^2]}\right\}, \tag{1.6}$$

where E_0 is the real amplitude of the field; F is the focal distance of the mirror; and $E(0)$ and a are the field amplitude and the beam width on the mirror for $z = 0$ and $D = 2z/ka^2$. The parameter $\delta = ka^2/2F$ (the Fresnel number) shows which of the two processes (diffraction or geometrical convergence) dominates. According to (1.6), the field amplitude on the beam axis first increases, achieves maximum $E(0)\sqrt{1+\delta^2}$ for $D = \delta/(1+\delta^2)$, and then monotonically decreases. The beam width first decreases due to focusing, achieves its minimum value (the beam radius in the focal plane $r_f = a/\sqrt{1+\delta^2}$) and then monotonically increases for $D > \delta/(1+\delta^2)$. If the Fresnel number is large, the minimal beam size is smaller than the initial amplitude by a factor of δ.

The known expressions obtained above show that the quasi-wave approximation well describes both the diffusion and refraction (see below) of electromagnetic radiation. The method of geometrical optics, which also describes the refraction of laser radiation, is restricted by the case of nonintersecting beams.

1.1.2 Propagation of Laser Radiation in Gases and Plasma

Due to the relatively high power of CO_2 lasers, the propagation of their radiation is often accompanied by nonlinear effects caused mainly by the formation of a "thermal lens" in the medium absorbing part of the laser beam energy.

The linear absorption coefficient for the $\lambda = 10.6\,\mu\text{m}$ CO_2 laser radiation in dry pure air at the atmospheric pressure at $T = 300\,\text{K}$ is determined by the interaction of radiation with carbon dioxide gas molecules and is quite small, $\mu = 0.072\,\text{km}^{-1}$ [2]. Gases in which laser radiation can propagate can differ significantly from pure dry air and can contain impurities of water, carbon dioxide, aerosols, etc. These impurities can enhance the absorption coefficient μ by many orders of magnitude. Here, we will consider for simplicity the propagation of laser radiation in pure dry air. The final expressions for other gases have the same form and can be easily obtained by the corresponding recalculation. The propagation of high-power CO_2 laser radiation has been studied in many papers. Here, we present the summary of the results [3, 4].

An initially focused laser beam (φ is the focusing angle) broadens due to thermal defocusing. Its minimal diameter is

$$d_1 = d_0 \exp(-\varphi^2/\varphi_0^2),\ \varphi_0^2 = \alpha_1 \mu P/2\pi\kappa \tag{1.7}$$

where d_0 is the mirror diameter; κ is the heat conductivity of air; α_1 is the proportionality coefficient in the expression for the refractive index of air $N = 1 - \alpha_1 T$ and T is the air temperature.

The distance at which the laser beam is spread due to defocusing to the width equal to the initial beam diameter $d_0 = 2R$ can be estimated from (1.7) as

$$z^* \approx R\sqrt{2\pi\kappa/\alpha_1 \mu P} \tag{1.8}$$

Let us make the estimate for air [$\kappa = 4 \times 10^{-4}\,\text{W/(cmK)}$, $\mu \approx 10^{-6}\,\text{cm}^{-1}$, $\alpha_1 \approx 10^{-6}\,\text{K}^{-1}$]. By assuming $R \approx 5\,\text{cm}$, we obtain $z^* \approx 2.5/\sqrt{P}$, where z^* is expressed in km and P in W. For example, a 10 kW parallel laser beam broadens twice at a distance of 25 m from a mirror.

The calculation of the thermal defocusing of a horizontally propagating beam may require the consideration of thermal convection, which results in the bending of the beam downwards towards a rising convective flow [see (1.10)] and in the decrease of the defocusing beam diameter due to convective cooling [5].

Let us assume that the transverse radiation intensity distribution on the mirror has a "hole" in the middle. Then, the air temperature distribution at the initial instant of time will be inhomogeneous, with a hole in the middle. Due to bending in heated regions, the inner beams will be focused on the axis, i.e. self-focusing appears. Later, the temperature of the heated gas will achieve its maximum at the beam center, and self-focusing will disappear. Self-focusing can exist during the time $\tau \approx R^2/4\chi$. This time in gas proves to be quite large. The thermal diffusivity of air is $\chi = 0.3\,\mathrm{cm}^2/\mathrm{s}$; for $R \approx 5\,\mathrm{cm}$, we have $\tau \approx 25\,\mathrm{s}$. In the case of the parabolic intensity profile, the initially parallel beams intersect at one point

$$z^{**} = R\sqrt{c_p\rho/\alpha_1\mu q_0 t} \tag{1.9}$$

(c_p and ρ are the specific heat and density of gas), which approaches the mirror with time. In air for $R = 5\,\mathrm{cm}$, we have $z^{**} = 15/\sqrt{tP}$, where z^{**} is expressed in km and P in W. For example, for $P = 10\,\mathrm{kW}$ and $t \approx 25\,\mathrm{s}$, the focus will be located at a distance of 30 m from the mirror.

Some technological operations require sometimes the blowing off of a sample by a gas flow. This can be related to the necessity of sample protecting or cooling.

A transverse (with respect to the beam axis) gas flow displaces the region of minimal density in the same direction and deflects the light beam. At the same time, gas cooling caused by this flow reduces thermal defocusing [2]. The beam bending and defocusing are also observed during processing of large surfaces by a scanning beam.

Calculations [3] show that in this case the focal point shifts upstream by the distance

$$d = 4\alpha_1\mu P/\pi c_p\rho v\varphi^2. \tag{1.10}$$

For example, for $\varphi = 10^{-3}$ and $v = 1\,\mathrm{m/s}$ in air, we obtain from (1.10) $d = 4 \times 10^{-5}P$, where d is expressed in cm and P in W. For $P = 2\,\mathrm{kW}$, the displacement of the focus is ~1 mm, which exceeds the typical focal spot diameter of an industrial CO_2 laser. The calculation of radiation defocusing in a medium containing aerosols is complicated by the photorefractive effect for sol particles, which is quite complicated.

The bleaching of gas containing a suspension of liquid aerosols caused by the evaporation of drops during the propagation of a CO_2 laser beam was calculated in [6].

The main specific feature of the propagation of light in a medium with free charge carriers is related to another mechanism of the interaction light with medium. While the propagation of light in air is determined by a decrease in its density caused by heating, the interaction of light with plasma is determined by the motion of conduction electrons in the wave field. The plasma permittivity is well known [7]:

$$\varepsilon = 1 - \frac{\omega_p^2}{\omega(\omega + i\nu)} = \varepsilon' + \mathrm{i}\varepsilon'',$$

$$\varepsilon' = 1 - \frac{\omega_p^2}{(\omega^2 + \nu^2)}, \quad \varepsilon'' = \frac{\omega_p^2 \nu}{\omega(\omega^2 + \nu^2)}, \tag{1.11}$$

where ν is the frequency of collisions of electrons with plasma atoms and ions and $\omega_p = 4\pi n_e e^2/m$ is the plasma frequency. The imaginary part ε'' of the permittivity is determined by the absorption coefficient μ of light in plasma:

$$\mu = k\varepsilon'' = \frac{\omega_p^2 \nu}{(\omega^2 + \nu^2)c}. \tag{1.12}$$

By substituting the real and imaginary parts of the permittivity from (1.11) and (1.12) into (1.5), we obtain the equation for the propagation of radiation in plasma:

$$-2ik\frac{\partial E}{\partial z} + \Delta_\perp E + k^2\left(-\frac{n}{n_c} + i\frac{\mu}{k}\right)E = 0 \tag{1.13}$$

where $n_c = (\omega^2 + \nu^2)m_e/4\pi e^2$ is the critical plasma density at which the real part of ε vanishes. For a CO_2 laser, $n_c \approx 10^{19}\,\mathrm{cm}^{-3}$.

The concentration n_e of free electrons in a plasma plume produced sometimes during laser processing of materials, is an equilibrium function of temperature. In the isobaric case (continuous optical discharge), the dependences of n_e and μ for different materials are presented in Figs. 3.3 and 3.4. One can see that, unlike air, the value of μ for plasma is quite large: $\mu \approx 1\,\mathrm{cm}^{-1}$. Therefore, it is necessary to take into account the attenuation of light due to absorption during propagation in plasma.

To describe the behavior of a laser beam in the optical discharge plasma, we will neglect first its attenuation and consider the propagation of beams assuming that the function ε' is specified. Considering only a plane case and using the geometrical optics approximation [4], we can obtain the equation for beam paths. For a beam focused at the point $z = F$, we have

$$x = (1 - z/F)x_0 + \frac{1}{4}z^2\frac{\partial}{\partial x}\varepsilon'\Big|_{x=x_0} \tag{1.14}$$

where x_0 is the coordinate of an elementary beam for $z = 0$ (on a lens or mirror). It is known that the equilibrium concentration of isobaric plasma is a rapidly increasing function of temperature. However, when the complete single ionization is achieved at $T = T^*$, the plasma density decreases due to the escape of particles from the heated region (see Fig. 3.3). If the plasma temperature $T_{\max}$ on the beam axis is lower than T^*, then $\partial\varepsilon'/\partial x > 0$ due to the decrease of temperature at the beam boundary. For $T_{\max} > T^*$, the function $\partial\varepsilon'/\partial x$ changes its sign at the point $T_{\max} = T^*$. One can see from (1.14) that the beams can be focused at one point only if the condition

$$\partial\varepsilon'/\partial x = \gamma x, \ \gamma = const$$

is fulfilled. By using (1.14), we can obtain the expression for the displacement ΔF of the focus in plasma:

$$\Delta F/F = \gamma\ F^2/4,\ |\Delta F| < F \tag{1.15}$$

It follows from (1.15) that, if $\gamma > 0$, the focus sifts along the beam due to defocusing. If $\gamma < 0$, the self-focusing of the beam takes place and the focus shifts towards the lens. The requirement of beam focusing at one point is difficult to fulfill because a parabolic dependence of ε' on the transverse coordinate is needed. The latter is unlikely. Indeed, we have

$$\frac{\partial \varepsilon'}{\partial x} = \frac{\partial \varepsilon'}{\partial T}\frac{\partial T}{\partial x}$$

In a continuous optical discharge, $\partial T/\partial x \sim x$ (see Sect. 3.3). As mentioned above, the quantity $\partial \varepsilon'/\partial T$ drastically depends on temperature. Therefore, in the general case the beams intersect at different points, the peripheral beams being deflected stronger because temperature at the plume periphery is lower and $\partial \varepsilon'/\partial T$ is higher than that at the beam axis. Thus, the beam shape should be distorted, i.e. aberration should be observed.

The displacement of the focus and the change in the focusing angle of light in plasma can be easily obtained from (1.11) and (1.15):

$$\Delta F/F = \frac{1}{4}\frac{n_{e\,\max}}{n_c \varphi^2},\ \varphi = R/F \tag{1.16}$$

$$\frac{\Delta \varphi}{\varphi} = -\frac{1}{4}\frac{n_{e\,\max}}{n_c \varphi^2}$$

It follows from (1.16) that the focus should draw aside from the lens with increasing power, while the focusing angle should decrease because the plasma temperature increases. The maximum density of the continuous optical discharge plasma in air at the atmospheric pressure is $n_{e\,\max} = 2 \times 10^{17}\,\mathrm{cm}^{-3}$ (see Sect. 3.1). Therefore, for $2\varphi \approx 0.1$, we have $\Delta\varphi/\varphi \sim |1|$. It follows from this that refraction can be considerable. Therefore, the theoretical problem of propagation of laser beams in plasma should be solved simultaneously for functions ε and E. This problem was solved in Chap. 3, where an optical discharge was investigated. In this chapter and in other chapters, the results of experiments on laser processing of materials are also described. Below, we will describe experiments on the refraction of a laser beam in the breakdown plasma in air. Although the experimental conditions strongly differ from the laser technology conditions, the results of measurements are clear and well illustrate the described phenomenon.

The refraction of a laser beam propagated through the optical breakdown plasma in the atmospheric air was measured in [8]. Experiments were performed by using a pulsed CO_2 laser. The pulse shape was typical for such lasers and consisted of a

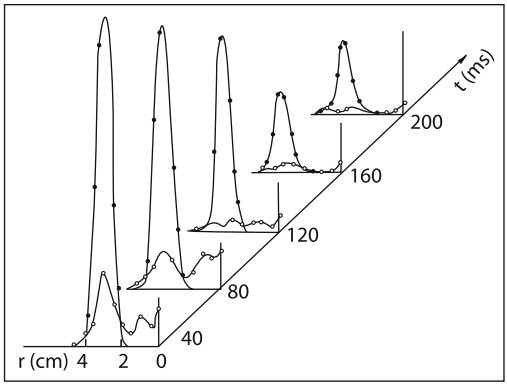

Fig. 1.1 Spatiotemporal laser radiation intensity distribution: (•) the initial distribution; (○) distribution after the breakdown

leading peak of duration $\tau_1 \sim 50$ ns and a tail of duration $\tau_1 \sim 2\,\mu$s. The radiation was focused by a metal mirror with the focal distance $F = 10$ m. An unstable resonator generated light in the form of a ring with the external diameter 10 cm and the internal diameter 6.5 cm. The radiation intensity in the focal spot was $q = 5 \times 10^8$ W/cm^2 for the total energy of the light pulse $E \approx 150$ J. This radiation intensity in the dusty atmosphere was sufficient to produce the optical breakdown of air. The radiation intensity propagated through the optical discharge was measured with a germanium detector at a distance of 7 m behind the focal plane. Figure 1.1 shows the radial intensity distribution at different instants. One can see that the initial beam is strongly absorbed and is spread towards the ring center.

1.2 Absorption, Reflection, and Propagation of Radiation in Cavities in Condensed Media

In this section, we consider an important quantity for laser technologies – the coefficient of light reflection from materials. The main attention will be devoted to the reflection of light from metal surfaces.

1.2.1 Flat Surface

It is known that the reflection coefficient for light normally incident from vacuum on a flat surface is described by the Fresnel formula [9]

$$R = |(\sqrt{\varepsilon} - 1)/(\sqrt{\varepsilon} + 1)|^2 \tag{1.17}$$

Permittivity of metals, as for plasma, is determined by free electrons, i.e. it can be calculated from (1.11), where ν is the frequency of scattering of electrons by the

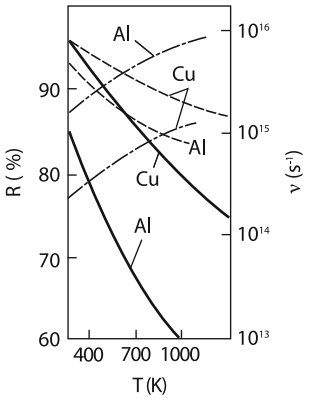

Fig. 1.2 Calculated temperature dependences of the reflectance R for laser radiation for wavelengths 1.06 μm (*solid line*) and 10.6 μm (*broken curves*) and the electron–phonon collision frequency ν (*broken point*)

thermal vibrations (phonons) of a lattice. The typical values for metals are $\omega_p \approx 10^{16}\,\mathrm{s}^{-1}$, $\nu \geq 10^{14}\,\mathrm{s}^{-1}$ (Fig. 1.2). While $\varepsilon'' \approx |\varepsilon' - 1| \approx 1$ for the optical discharge plasma, in metals for the CO_2 laser radiation, we have ε', $\varepsilon'' \approx 10^4$, i.e. $R \approx 1$. For most metals, especially at high temperatures, $\nu \gg \omega$ (Fig. 1.2), and therefore, as follows from (1.11), $\varepsilon'' \gg \varepsilon'$. In this approximation, we obtain from (1.17)

$$R = 1 - \sqrt{8/\varepsilon''}$$

By expressing ε'' in terms of the conduction $\sigma = n_e e^2/\nu m$ as $\varepsilon'' = 4\pi\sigma/\omega$, we obtain finally

$$R = 1 - \sqrt{2\omega/\pi\sigma} \tag{1.18}$$

Thus, the reflection coefficient R of a material is determined only by its conduction. In [10], the reflection coefficient R was calculated by (1.17) taking into account the temperature dependence for different laser wavelengths (see Fig. 1.2). In [11], the values of the absorption coefficient $\alpha = 1 - R$ are presented in a broader temperature range (Fig. 1.3). The temperature dependence of the conduction can be also estimated by using the known empirical relation for the specific resistance ρ

$$\rho = \rho_0(1 + \alpha_T T)$$

where ρ_0 is the specific resistance at $T = 0°\mathrm{C}$ and α_T is the temperature resistance coefficient. By substituting this expression into (1.18), we obtain the temperature dependence of α. For $T < \alpha_T^{-1}$, the increment of α will depend linearly on temperature (the Drude model). For example, $\alpha_T = 6 \times 10^{-3}\,\mathrm{C}^{-1}$ for iron, which means that α will increase linearly with temperature up to ~500 K. At higher temperatures of the metal, $\alpha \propto \sqrt{T}$, which is demonstrated in Fig. 1.3a.

It is know that the wavelength of light in a medium decreases by a factor of N compared to vacuum, where $N = \sqrt{|\varepsilon|}$ is the refractive index of the medium. In the case of $\nu \gg \omega$, the wavelength of light in a metal is $\delta = c/\omega\sqrt{\varepsilon} = \sqrt{c^2/4\pi\sigma\omega}$.

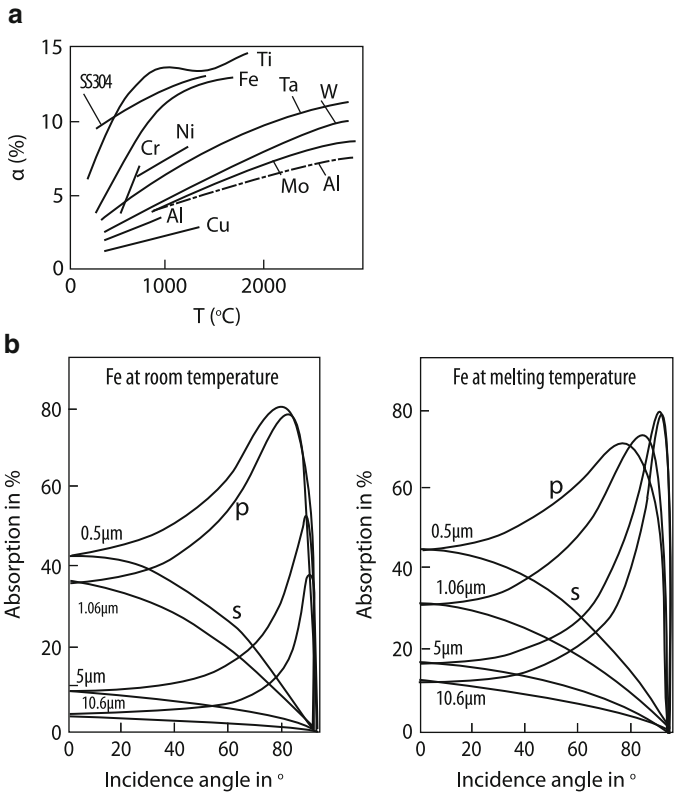

Fig. 1.3 Temperature dependences of the absorption coefficient of various materials at the CO_2 laser wavelength (**a**). Dependences of the absorption coefficient of iron on the angle of incidence, polarization, and wavelength at room temperature (*at the left*) and at the melting temperature (*at the right*) (**b**)

The skin depth[1] δ is very small because $\varepsilon \gg 1$. In this case, expressions for the reflection coefficients of light with different polarizations are rather simple [9]:

$$R_{\perp} = 1 - 4\xi' \cos\theta_0 \tag{1.19}$$

$$R_{\parallel} = |(\cos\theta_0 - \xi)/(\cos\theta_0 + \xi)|^2 \tag{1.20}$$

where $\xi = \xi' + i\xi'' = (1 - i)\sqrt{\omega/8\pi\sigma}$ is the surface impedance of the metal; θ_0 is the angle of incidence of light; $R_{\perp}$ and $R_{\parallel}$ are the reflection coefficients for a wave with the electric field vector normal or parallel to the plane of incidence. In the case of normal incidence, $R_{\perp}$ is equal to $R_{\parallel}$ and coincides with (1.18). As the angle of

[1]The wavelength of light in a metal is at the same time the penetration (skin) depth of the field [9].

incidence is increased (i.e. on passing to grazing incidence), $R_\perp$ increases, while $R_\parallel$ decreases. For θ_0 not too close to $\pi/2$, we have

$$R_\parallel = 1 - 4\xi'/\cos\theta_0 \tag{1.21}$$

For $\theta_1 = \pi/2 - \theta_0 = |\xi|$, $R_\parallel$ has a minimum equal to $(\sqrt{2}-1)/(\sqrt{2}+1)$. In this case, $\alpha = 1 - R$ achieves the maximum value equal to 83%, and the grazing angle is $\theta_1 \sim 10^{-2}$. Figure 1.3b shows the dependences of the absorption coefficients of iron on the angle of incidence for light beams of different polarizations at the surface temperature equal to the room and melting temperature [12]. One can see that these dependences are similar in a broad wavelength range.

All the expressions for reflection coefficients are applied for pure, polished surfaces. For materials with unpurified and unpolished surfaces (supplied materials), the absorption coefficient depends on the surface state and can considerably exceed α for pure surfaces (Table 1.1) [13].

Note that upon heating of samples up to comparatively high temperatures, contaminants on the surface can be burned out and the roughness can disappear (upon melting). Therefore, if oxidation or other chemical processes do not occur at high temperatures, the absorption coefficient will be close to its value for a pure metal. The absorption coefficient can be increased artificially. It is especially important for the CO_2 laser radiation because $\alpha \leq 0.1$ at a wavelength of $\lambda = 10.6\,\mu$m. To increase the absorption coefficient, the surface of a sample is covered with special heat-resistant materials absorbing IR radiation, for example, zinc phosphate, which has the effective absorption coefficient $\alpha_e = 0.7$ at $T = 1{,}000$°C [14]. This question will be considered in more detail in the discussion of laser hardening in Sect. 2.1.

The absorption coefficient can increase with increasing the surface temperature if heating is performed in an oxidizing atmosphere (for example, in air [15]). As an oxide film grows, the absorption coefficient periodically increases when the film thickness becomes multiple of half the wavelength of light. Thus, α_e oscillates in time (Fig. 1.4a,b), as it occurs on a copper target, where melting proceeds quite

Table 1.1 Absorption coefficient α at $\lambda = 10.6\,\mu$m, (%)

Material	Unpurified and unpolished surface	Polished surface
Stainless 316 steel	39	9
Stainless 416 steel	42	10
Aluminum	12	2
Copper	12	2
4130 steel	85	
Molybdenum	12	3
Tantalum	21	4
Silver	–	1
Gold	–	1
Rhodium	–	4

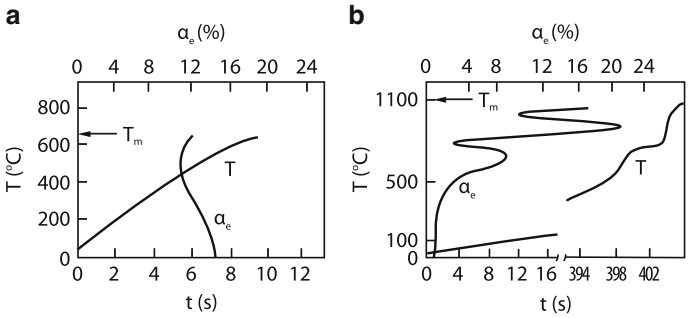

Fig. 1.4 Characteristic heating curves for thermally thin targets heated in air by the CO_2 laser radiation for $P = 30$ W and $q = 1.3$ kW/cm^2 and the corresponding effective absorption coefficients α_e: (**a**) duralumin ($m = 54$ mg); (**b**) copper ($m = 116$ mg)

actively. One can see from Fig. 1.4b that due to oxidation the absorption coefficient for a pure surface can be an order of magnitude higher. The situation is different when the aluminum surface is heated (Fig. 1.4a). In this case, the oxide film is very strong, and its thickness does not grow with time. The effect of laser-induced combustion of a metal surface is quite similar to the oxidation of a metal surface in the laser field. As many exothermal chemical reactions, the burning of a metal in a laser beam in an oxidizing atmosphere has a threshold and appears abruptly. Processes of laser thermal chemistry are described in detail in [15]. The oxidation of a metal surface plays a significant role in laser cutting of metals in the oxygen atmosphere (see Chap. 5).

1.2.2 Propagation of Laser Radiation in a Narrow Channel in a Metal

Some types of laser processing of materials (cutting, welding, drilling, see Chaps. 4, 5, and 8) require a deep penetration of the laser beam into material. In this case, the radiation intensity should be high enough. In this connection, it is often necessary to obtain the minimal size of a laser spot on the target surface. According to (1.6), the focal spot radius is $r_f \simeq \lambda/\varphi$, i.e. it is inversely proportional to the focusing angle φ. Therefore, it is necessary to use tightly focused radiation. But such radiation will be defocused behind the focal plane (usually coincident with the sample surface plane) already at a small depth $L \approx \lambda/\varphi^2$ and will fall on the side walls of the channel. If the absorption coefficient α is large (radiation is short-wavelength with parallel polarization), defocusing reduces a part of energy released at the channel bottom. If α is small, the greatest part of light will be reflected from the walls and fall to the bottom. Multiple reflections are especially important for normally polarized radiation for which the reflection coefficient increases with increasing the angle of incidence [(1.19), Fig. 1.3b]. During laser welding, cutting, and drilling,

it is necessary to know the light intensity distribution in the channel because it determined the dynamics and efficiency of these processes.

The light distribution in the cannel can be relatively simply calculated in the geometrical optics approximation or waveguide approximation. An elementary light beam multiply reflected from the channel walls is either completely absorbed, if the channel is deep, or comes back, if the channel is shallow and melting is not through. If the beam is not spread due to diffraction to the width exceeding the channel width d, its behavior can be described within the framework of geometrical optics; otherwise, the beam propagation has the waveguide nature. We will assume for simplicity that radiation at the channel input is incoherent (for example, radiation from a multimode laser). In this case, it is convenient to describe radiation as a photon flux. Let us assume that the intensity distribution of light incident on a keyhole is bell-shaped. Due to limitedness of the beam, it has the angular spread $k_\perp/k \simeq \lambda/d$. Due to diffraction, the elementary beam is spread at the keyhole bottom up to the width $\lambda h/d$. To calculate the beam trajectory, this width should be smaller than the channel width d, as mentioned above. This gives the condition of the applicability of the geometrical optics approximation:

$$d^2/\lambda h \gg 1$$

Thus, the geometrical optics approximation is valid for large Fresnel numbers.

This inequality can be rewritten by introducing the channel aspect ratio h/d coinciding with the weld aspect ratio (see Chap. 4):

$$d/\lambda \gg h/d$$

In practice, $h/d \approx 5$–10, i.e. for $\lambda = 10.6\,\mu$m, the theory can be applied if $d \geq 0.1$ mm. The geometrical optics approximation is convenient in the case of shallow keyholes, when photons experience a small number of reflections and the reflected power is $P_r \sim P$ (in this case, the waveguide approximation is not valid).

In the geometrical optics approximation, the focused radiation can be represented by a set of N beams [16]. We assume that the angular distribution of beams at the focus is described by a Gaussian

$$f(\varphi) = \frac{N}{\pi\varphi_0^2}(2\pi)^\nu \exp(-\varphi^2/\varphi_0^2)$$

where $\varphi_0 < \pi$ is the focusing angle; $\nu = 0$ in the axially symmetric case and $\nu = 1$ in the plane case. Figure 9.45 presents the scheme of incident beams. The power of each beam at the input to the keyhole is P/N, where P is the laser power. The trajectory of each beam in the keyhole was numerically calculated by multiplying the power of each beam after the next reflection from the wall by the reflection coefficient calculated from (1.19) and (1.20) [16]. If the beam power became 10^4 times lower, the beam was excluded from consideration. The energy absorbed by a

given element of the keyhole surface was calculated by summation of contributions from individual beams.

The dependence of the effective absorption coefficient $\alpha_e = (P - P_r)/P$ on the keyhole depth were numerically calculated by thus method. The absorption coefficient α_e increases with increasing the keyhole depth having a parabolic profile (Fig. 1.5). As expected, radiation with parallel polarization is absorbed more efficiently because the absorption coefficient α for this radiation is higher. The calculations were performed for steel with $4\xi' = 0.1$. It was assumed that a laser emits plane-polarized radiation with the electric vector directed either along a slit or across it. The focusing angle of light was $\varphi_0 = 30°$. In the case of an axially symmetric keyhole, calculations were performed for laser radiation with circular or radial polarization (Fig. 5.22). The effective absorption coefficient for laser radiation measured upon laser welding behaves similarly to the calculated α_e, increasing with increasing h/d and achieving unity for a large depth of the vapor-gas channel (Fig. 4.9).

Consider now the depth distribution of radiation intensity absorbed by keyhole walls. If the channel were cylindrical, the intensity of circularly polarized radiation

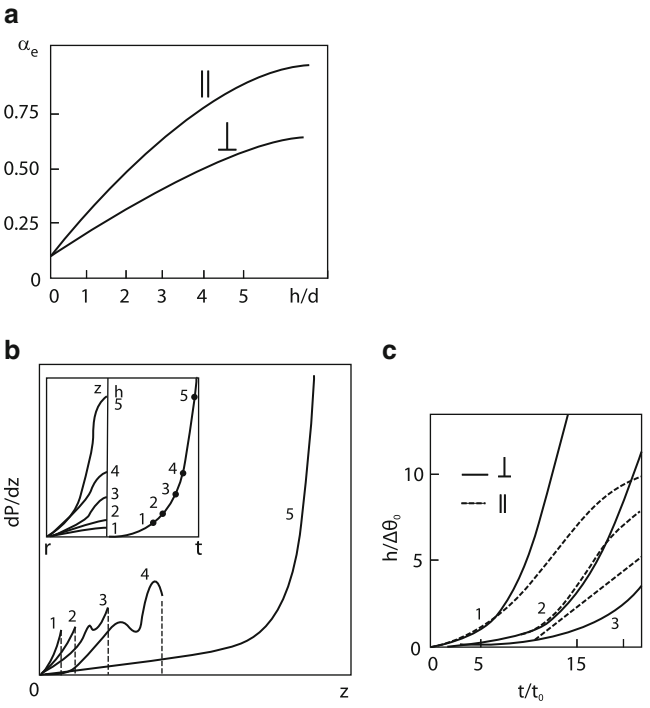

Fig. 1.5 Dependence of the effective absorption coefficient α_e of a steel target for the CO_2 laser radiation on the keyhole depth (the focusing angle is $\varphi = 30°$, $\alpha = 0.1$; $\parallel$ and $\perp$ are parallel and normal polarizations of light (**a**). The dependence of the radiation power dP/dz absorbed by the walls on the coordinate z inside each keyholes during drilling (**b**). The depthes of keyholes vs time at different polarization (**c**). Details in Chap. 8

absorbed by the walls would decrease with increasing depth. In the case of radial polarization, the situation is more complicated. At the same time, if absorption by walls were absent, the radiation intensity should increase with approaching the keyhole bottom due to the channel narrowing. This is illustrated by the elementary consideration of the paths of beams in a cone. Figure 1.5b demonstrated that both these tendencies are manifested in the calculation of the radiation intensity absorbed by the walls. This figure shows the keyhole shapes observed at subsequent instants of time during drilling of steel by radially polarized radiation from a CO_2 laser (see details in Chap. 8). The dependence of the radiation power $\mathrm{d}P/\mathrm{d}z$ absorbed by the walls on the coordinate z inside each keyhole is shown below. One can see that this power depends on the coordinate z and keyhole shape in a complicated way. Near the turning point of a group of beams propagating at an angle of $\varphi \sim \varphi_0$, a local maximum appears. As the keyhole depth further increases, the number of maxima increases and their amplitude increases. Finally, they merge to form one maximum located near the keyhole bottom (see curve 5 in Fig. 1.5b).

1.2.3 Waveguide Radiation Propagation Regime

The propagation of laser radiation in a deep narrow channel can be described as the propagation of radiation in a waveguide (with diameter slowly varying along its length and in time). It is known [9] that electromagnetic waves of two types (the E and H waves) can propagate in such a waveguide. The E wave will be excited when laser radiation is polarized along the beam radius (see Fig. 5.22). The attenuation coefficient of such modes in a waveguide with a circular cross section is [9]

$$\alpha_E = \alpha/2r, \tag{1.22}$$

where r is the waveguide radius. The H waves with the vector E parallel to the side wall of the waveguide are attenuated as the E waves (see Fig. 5.22). However, the absorption coefficient of the lowest H_{01} mode (without zeroes over the azimuthal angle) is very small:

$$\alpha_H = \frac{\alpha}{2r}(kr)^{-2},$$
$$kr = 2\pi r/\lambda \gg 1. \tag{1.23}$$

Knowing the absorption coefficient, we can write the equation describing the propagation of radiation in the waveguide regime:

$$\mathrm{d}P/\mathrm{d}z = -\alpha_{E,H} P, \tag{1.24}$$

where z is measured from the channel entrance towards its bottom. It is assumed in (1.24) that the bottom is located far from the channel entrance $h \gg 1/\alpha_{E,H}$ so

that radiation reflected from the bottom can be neglected. By integrating (1.24), we obtain the dependence of the radiation intensity q_n absorbed by the walls on z for the E mode:

$$q_n = \frac{\alpha P_0}{4\pi r^2(z)} \exp\left[-\int_0^z \alpha \mathrm{d}z/2r(z)\right]. \tag{1.25}$$

Thus, $q_n(z)$ depends on α and the shape of the channel $r(z)$. Below, we will use (1.24) for calculating analytically laser drilling and an optical discharge in a channel (see Chaps. 3 and 8).

One or other type of modes can be excited in the channel by selecting the required polarization of a laser beam. As mentioned above, to excite the E wave, the electric field vector of the incident laser beam should be directed along the radius. For H wave the electric field vertor should be directed along the azimut. Note that the waves of both types are also excited in the case of plane-polarized incident beam, but their intensity ratio depends on the geometry and parameters of the problem. The radial or azimuthal polarization is obtained by inscribing corresponding grooves on mirrors of the CO_2 laser resonator (Fig. 1.6) [17]. In this way, it is possible to obtain the degree of polarization ~50%: the nonpolarised TEM_{00} mode and radially polarized TEM_{01} mode (the TEM_{00} has no zeroes both over r and z, the TEM_{01} mode has no zeroes over r and has zeroes over φ). The laser beam power of ~2 kW was typical for laser technology. Laser beams with such polarization are of interest not only for excitation of required waves in deep keyholes. In a number of problems, for example, in the description of gas-laser cutting such beams are used "directly" because due to a small number of reflections a keyhole weakly affects the laser beam structure. This is discussed in more detail in Chap. 5. It is clear that radially or axially polarized beams excite waves of the same polarization in a keyhole. But what will be the picture when the incident beam is plane-polarized? Such polarization is used in experiments most often. Before considering this situation, note that because this problem is quite complicated, a cylindrical keyhole is usually studied theoretically. The shapes of a vapor-gas keyhole in laser technologies strongly differ from cylindrical. In a better case, for example, during laser drilling a keyhole represents an axially symmetric deep hole resembling a cone. A keyhole

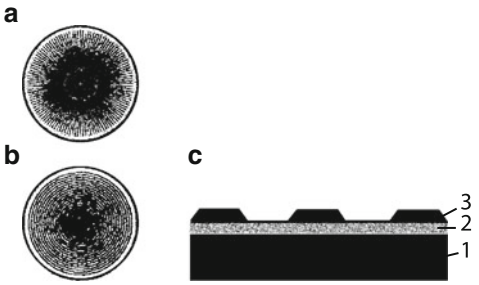

Fig. 1.6 Structure of grooves on optical elements for generating radially (**a**) and azimuthally (**b**) polarized radiation. The structure of an optical element (**c**): (**1**) silicon substrate, (**2**) Ti adhesion layer, (**3**) reflecting copper layer

in a welding pool has the three-dimensional geometry. It was shown experimentally [18] that the deviation from the cylindrical shape of the channel strongly affects the transmission of radiation through the channel. The problem is also complicated by the fact that the keyhole walls can be rough for a number of reasons. Thus, it is still prematurely to hope to describe adequately the propagation of radiation in real keyholes. Nevertheless, to study this effect qualitatively, it is reasonable to consider excitation of waves in a cylindrical keyhole by a plane-polarized beam.

1.2.4 Propagation of Plane-Polarized Radiation in a Cylindrical Keyhole

It is impossible to perform detailed measurements of absorption coefficients under real conditions of laser technological processes, and therefore we will consider only model experiments. Low-power radiation was incident coaxially on the input of cylindrical tubes of small diameter 0.5–1 mm (Fig. 1.7). The converging angle of a plane-polarized beam could be varied in a broad range with the help of a telescopic system. Figure 1.8 presents the dependences of the logarithm of radiation transmission on the ratio of the tube length to its internal diameter [19]. The straight lines fitting experimental points demonstrate the exponential decay of laser radiation in thin capillaries. The attenuation coefficient increases with increasing the converging angle φ of the laser beam.

We will describe the excitation of waves in a metal capillary by the method used for solving problems in waveguides [20]. The electric and magnetic field vectors are expressed in terms of scalar functions – the Hertz potentials [21]. This problem is cumbersome as a whole. To give only the general picture of the phenomenon, we consider only the formulation of the problem and results of its solution. The Hertz

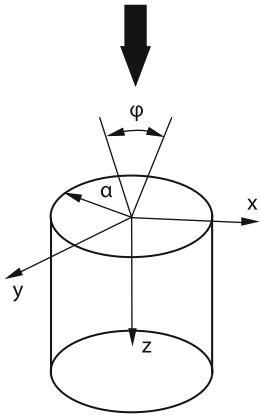

Fig. 1.7 Scheme of the propagation of radiation in a waveguide

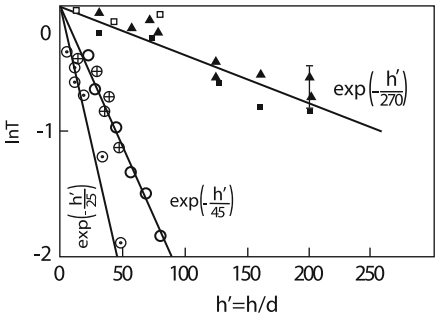

Fig. 1.8 Experimental dependencies of the logarithm of transmission of tubes on the reduced length: (*ring with cross*) Cr, $d = 1$ mm, $\theta = 0.05$; (*square*) Cr, $d = 1$ mm, $\theta = 0.003$; (*ring*) stainless steel, $d = 0.5$ mm, $\theta = 0.05$; (*dark ring*) German silver, $d = 0.78$ mm, $\theta = 0.05$; (*black square*) German silver, $d = 0.78$ mm, $\theta = 0.003$; (*triangle*) German silver, $d = 0.78$ mm, $\theta = 0.005$; (*ring with point*) German silver, $d = 0.78$ mm, $\theta = 0.12$

potentials satisfy the equations [21]:

$$\begin{aligned} \mathrm{i}\frac{\partial \Pi}{\partial z} + \frac{1}{r}\frac{\partial}{\partial r}\left(r\frac{\partial \Pi}{\partial r}\right) - \frac{m^2}{r^2}\Pi = 0, \\ \mathrm{i}\frac{\partial \tilde{\Pi}}{\partial z} + \frac{1}{r}\frac{\partial}{\partial r}\left(r\frac{\partial \tilde{\Pi}}{\partial r}\right) - \frac{m^2}{r^2}\tilde{\Pi} = 0, \end{aligned} \tag{1.26}$$

where $m = 0, 1, 2$, is the azimuthal number. The cylindrical dimensionless variables are $r \to r/a$ and $z \to z/2\kappa a^2$. Due to the smallness of the impedance $|\xi| \ll 1$, the boundary conditions on the walls are selected by using the Leontovich conditions:

$$\begin{aligned} \frac{\partial \Pi}{\partial z} = -\xi\kappa a\left(\frac{\partial \Pi}{\partial z} - \tilde{\Pi}\frac{m}{r}\right), \\ \frac{\partial \tilde{\Pi}}{\partial z} = -\frac{\kappa a}{\xi}\left(\frac{\partial \tilde{\Pi}}{\partial z} - \Pi\frac{m}{r}\right). \end{aligned} \tag{1.27}$$

The absence of singularities Π and $\tilde{\Pi}$ on the capillary axis gives additional conditions

$$r\left(\frac{\partial \Pi}{\partial r}\right) \to 0, \quad r\left(\frac{\partial \tilde{\Pi}}{\partial r}\right) \to 0, \quad r \to 0$$

The Hertz potentials at the capillary input for $z = 0$ for a linearly polarized laser beam with the electric field distribution $E_0(r)$ and $E_z = 0$ will satisfy the relations

$$\begin{aligned} \frac{\partial \Pi}{\partial r} - \frac{\tilde{\Pi}}{r} &= E_0(r), \\ \frac{\partial \tilde{\Pi}}{\partial r} - \frac{\Pi}{2} &= -E_0(r). \end{aligned} \tag{1.28}$$

The solution of system (1.26)–(1.28) is represented in the form of an exponential depending on z and Bessel functions of order m [20]. The numbers n of a mode determining zeroes over coordinates r and z depend on m. The structure of modes depends on relation between n and $|\zeta|\kappa a$. When $n \gg |\zeta|\kappa a$, the E and H modes are excited, in the opposite case – superposition modes are excited. If $|\zeta|\kappa a \ll 1$, the entire mode composition is divided into the E and H modes. In the opposite limit, only highest modes are divided into the E and H modes. Each of the modes is characterized by its own attenuation coefficient. It usually increases with increasing n. Note here that $n = \kappa a\varphi$, i.e. the higher mode corresponds to the higher convergence angle of the incident laser beam. Thus, the absorption coefficient increases with increasing the convergence angle, which is observed in Fig. 1.8. For the same convergence angles, the attenuation coefficient of the E modes always exceeded that of the H modes. Note that at small converging angles for $\kappa a\zeta \gg 1$, mixed waves with the attenuation coefficient smaller than α_E are generated.

To perform quantitative comparison with calculations, a special experiment with the selected convergence angle was conducted. The mode composition and transmission of laser radiation were calculated numerically by (1.26), (1.28). The field at the input to a cylindrical tube was the result of diffraction of a linearly polarized wave from a circular aperture. The value of ζ was determined experimentally by measuring the absorption coefficient of the capillary material. The capillary transmission calculated numerically is presented in Fig. 1.9 for two converging angles [22]. In this case, $\zeta\kappa a \gg 1$, so that mixed waves with the attenuation coefficient that is considerably smaller than α_E correspond to small angles. According to (1.22), the attenuation length of the E mode under these experimental conditions is 2.5 cm, which is considerably smaller than attenuation lengths presented in Fig. 1.9. The agreement of calculations with the experiment confirms the validity of model (1.26). Note in conclusion that processes considered above are important

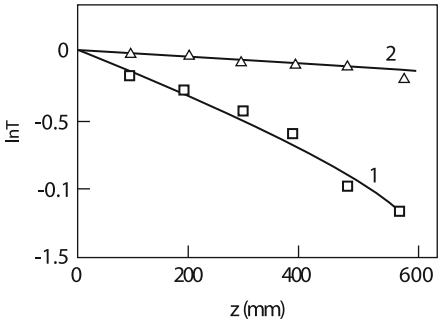

Fig. 1.9 Dependences of transmission on the length of a copper capillary of radius $a = 0.9$ mm for $\zeta = 0.02$–0.08. The capillary input is irradiated by a beam formed by a circular aperture. (1) $\varphi_1 = 0.019$, $\varphi_2 = 0.026$, $r_0 = 15$ mm, $\Delta r = 5$ mm; (2) $\varphi_1 = 0{,}003$, $\varphi_2 = 0$, $r_0 = 0$, $\Delta r = 2.5$ mm

for long-wavelength radiation, e.g., for practically important radiation of a CO_2 laser. For the wavelengths not exceeding 1 μm, a great part of radiation is absorbed already after the first reflection of beams from keyhole walls.

1.3 Physical Processes on the Surface of Condensed Media: The Interaction of Vapor with the Surrounding Gas

Consider processes on the surface of solids, which are important for laser processing of materials, at different radiation intensities. At low intensities, the surface will be only heated; at higher intensities, melting occurs[2] and as the radiation power density is further increased, evaporation begins. Surface heating processes are quite simple if the temperature dependence of the absorption coefficient is neglected. These questions will be discussed in detail in the consideration of laser hardening of materials in Chap. 2. Physical processes occurring during melting are more various.

1.3.1 Melting

One of the widespread processes is convection caused by gravitational forces in liquid heated from bottom (Benard convection). Because a sample is usually heated by a laser beam from above, such convection does not appear in this case. As was shown theoretically in [23], the Benard convection in a liquid layer can also appear (in the absence of the gravitational force) due to the temperature dependence of the surface tension. In this case, the sign of the temperature gradient is not important, i.e. convection appears upon heating from above as well [24]. Effects related to the liquid motion near the interface and caused by the dependence of the surface tension on temperature or impurity concentration are called Marangoni effects [25]. Thermocapillary convection in a thin liquid layer in the presence of the longitudinal temperature gradient was calculated in [26]. The motion of air bubbles in liquid caused by the Marangoni effect was observed in [27].

Based on the Navier–Stokes equations and the heat conduction equation (see Sect. 2.2), it was shown in [24] that, aside from usual gravitational-capillary waves $\omega_0 = (gk + \sigma k^3/\rho)^{1/2}$ [28], another type of undamped surface waves with the dispersion law of the sonic type $\omega = kc$, where $c^2 \sim \mathrm{d}T/\mathrm{d}z$ (thermocapillary waves) also exist in a liquid layer heated from above. The maximum increment γ_M is achieved in the resonance $\omega_0(k) = ck$, i.e. $k = k_1 = q|\partial\sigma/\partial T|/\kappa\sigma$, where σ is the surface tension coefficient and q is the radiation intensity absorbed by the surface. The value of γ_M is given by the expression

[2]Note that upon heating, a sample, remaining solid before melting, can experience a number of phase transitions; some such phase transitions during laser hardening are considered in Sect. 2.1.

$$\gamma_M \simeq \omega_0(k_1)/2$$

For $q \simeq 10^5\,\mathrm{W/cm^2}$, for steel $k_1 \simeq 10^2\,\mathrm{cm^{-1}}$ $\gamma_M \sim 10^3\,\mathrm{s^{-1}}$. Thus, the increment of this instability is quite large, and the instability can be observed during the melting of the sample by laser pulses of duration of a few milliseconds. It is possible that such instability was observed in experiments [29], where solidified waves are observed on the sample surface. In addition, such instability causes the mixing of liquid, which is important for laser alloying. The practical significance of this phenomenon is not clear enough because the nonlinear stage of the process has not been studied.

The Marangoni effect can be manifested when the limited size of the beam diameter is taken into account. In this case, the motion occurs at a large scale of the order of the light spot diameter on a target. This motion will be considered in more detail in Sect. 2.2.

1.3.2 Vaporization

Vaporization of materials irradiated by a focused laser beam takes places in many technological processes such as welding, drilling and cutting. Because the material vapor pressure rapidly increases with increasing the surface temperature, vaporization also appears very rapidly. Each material can be characterized by its vaporization threshold. If a sample is heated slowly enough, so that the heating time $t_h \gg r_f^2/4\chi$, the target surface temperature can be considered a function of the radiation intensity:

$$T_s = \alpha q r_f/\kappa$$

The vaporization threshold q_b can be found from the condition that the sample surface is heated up to the boiling temperature T_b:

$$\alpha q_b = \kappa T_b/r_f \tag{1.29}$$

Upon pulsed heating, the radiation intensity q_b producing boiling of the sample material at the pulse end can be found by replacing r_f by $2\sqrt{\chi\tau}$ in (1.29):

$$\alpha q_b \simeq \kappa T_b/2\sqrt{\chi\tau} \tag{1.30}$$

If $q \gg q_b$, the laser beam energy is completely spent to vaporize the sample material and the so-called vaporization wave is produced [30].

Due to the mass removal, the melt level under the laser beam lowers. The lowering velocity v_e (the vaporization wave velocity) can be easily found from the law of conservation of energy and mass:

$$\alpha q = L_b \rho v_e \tag{1.31}$$

where L_b is the enthalpy of the material unit mass at the boiling temperature (vaporization enthalpy). Generally speaking, this expression is valid for a broad beam, when the flowing of liquid in the lateral direction can be neglected (see Sect. 8.1).

1.3.3 Melting–Solidification Dynamics Taking Vaporization into Account

Formula (1.31) is a limiting expression for this case, which is valid within a long time after the onset of boiling. The boiling onset time depends on the radiation intensity and can be estimated from (1.30). To consider all the stages of heating, melting, vaporization, and passage to the stationary regime of the vaporization wave, it is necessary to solve the system of nonstationary heat conduction equations for a solid and melt:

$$\frac{\partial^2 T_l}{\partial x^2} = \frac{1}{\chi_l}\frac{\partial T_l}{\partial t},\ \frac{\partial T_s}{\partial x^2} = \frac{1}{\chi_s}\frac{\partial T_s}{\partial x^2} \tag{1.32}$$

$$q_0 = -\kappa_l \left.\frac{\partial T_l}{\partial x}\right|_{s_2} + \rho_l H_b \frac{\mathrm{d}S_2}{\mathrm{d}t} \tag{1.33}$$

$$\kappa_l \left.\frac{\partial T_l}{\partial x}\right|_{S_1} - \kappa_s \left.\frac{\partial T_s}{\partial x}\right|_{S_1} = -\rho_s H_m \frac{\mathrm{d}S_1}{\mathrm{d}t},\ T_l(x = S_1) = T_s(x = S_1) = T_m \tag{1.34}$$

$$\frac{\mathrm{d}S_2}{\mathrm{d}t} = V_* \exp\left(-\frac{mH_b}{k_\mathrm{B} T_l(S_2)}\right),\ V_* = p_0/2\rho_l\sqrt{2\pi\kappa T_a/m}\exp(H_b m/k_\mathrm{B} T_b) \tag{1.35}$$

where T_l and T_s are the temperatures of the melt and solid, respectively; x is directed from the sample surface inside it; m is the material atom mass; subscripts l and s refer to the parameters of the liquid and solid, respectively; and S_2 and S_1 are coordinates of the melt–vapor and melt–solid surfaces, respectively. The lowering velocity of the melt surface S_2 (1.35) is obtained from the Hertz–Knudsen vaporization law, where p_0 is the atmospheric pressure, and T_b is the boiling temperature. Figure 1.10 presents the time dependences of the melting (S_1) and vaporization (S_2) fronts of a titanium sample obtained by solving the system of (1.32)–(1.35) [41]. One can see that the dynamics of these fronts is different. The melting front velocity decreases and tends to a stationary value. The vaporization front velocity monotonically increases and also tends to a stationary value. A stationary vaporization-melting wave can appear only when the velocities of phase boundaries are identical. Note here that the melting depths taking into account vaporization and neglecting it are close. This is explained by the fact that the temperature gradient decreasing on the growing melting layer front is compensated due to a decrease in the melt thickness due to vaporization.

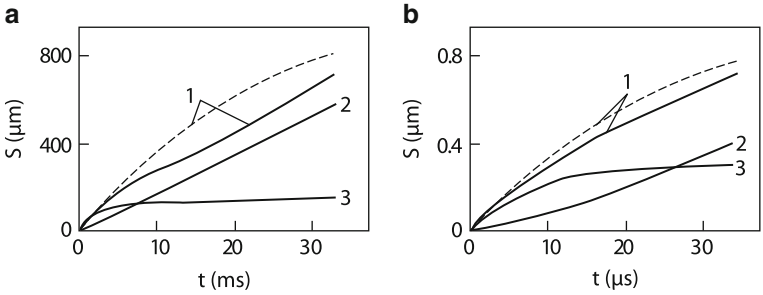

Fig. 1.10 Numerical calculations of thermal processes by laser irradiation $q = 10^5$ W/cm^2 (*left*), $q = 10^8$ W/cm^2 (*right*). Lines 1 are melting fronts, lines 2 are evaporation fronts, lines 3 are melt depthes. *Dash curves* are melting fronts without the evaporation

System (1.32)–(1.35) admits the self-modeling solution near the stationary state [58]:

$$v = q_0\{\kappa_s(T_m - T_0)/\chi_s + \kappa_l(T_a - T_m)/\chi_l + \rho(H_b + H_m)\}^{-1} \tag{1.36}$$

$$\Delta S = -\frac{\chi_l}{v}\ln\frac{\kappa_s(T_m - T_0)/\chi_s + \rho L_m}{\kappa_s(T_m - T_0)/\chi_s + \kappa_l(T_a - T_m)/\chi_l + \rho(H_b + H_m)} \tag{1.37}$$

$$T_a = -\frac{H_b m}{k_\mathrm{B}}\ln^{-1}\frac{v}{v_*} \tag{1.38}$$

Comparison of the self-modeling solution with the results of numerical simulation shows that they coincide with an accuracy of 5%. For $T_0 \ll T_m$, expression (1.36) coincides with (1.31). The thickness ΔS of the melt layer is determined, as expected, by the thickness of χ_l/v of a thermal wave, and depends logarithmically on thermal parameters. Taking into account that $H_b m \gg k_\mathrm{B} T_b$, one can see from (1.38) that the surface temperature T_a, as expected, is close to the boiling temperature T_b. As the laser radiation intensity is increased, the temperature T_a weakly (logarithmically) increases.

We considered above the simplest case of melting and vaporization of the surface of a thick metal sample. These processes can reveal interesting features when the interaction geometry is changed and a laser beam is focused in a small spot on a thin plate. In this case, the melt will be extruded on the edges of the melt pool under the action of vapor (see Chap. 8). Interesting properties can be observed when a thin metal plate is melted [58]. In this case, system (1.32)–(1.36) should be changed. Along with the energy loss due to vaporization, we introduce into (1.33) thermal losses described by the Stephan–Boltzmann law

$$q_\sigma = \varepsilon_1 \sigma T_a^4 \tag{1.39}$$

The same losses should be also introduced on the lower side of the plate:

$$-\kappa_s \frac{\partial T_2}{\partial x}\bigg|_{x=l} = \varepsilon_2 \sigma T_2^4 \tag{1.40}$$

Here, ε_1 and ε_2 are the radiation capacities of the upper and lower surfaces of the plate, respectively, and l is the plate thickness. Thermal radiation from the upper surface should be taken into account because the thermal story of the plate is considered after the laser switching off as well, when melting processes are changed by crystallization. Because radiation is focused into a small spot of radius r_f, temperature will change not only along the plate depth but also along its surface, i.e. along r. Therefore, equation (1.32) should be supplemented with a term describing heat transfer along the plate.

$$\kappa \frac{1}{r}\frac{\partial}{r}r\frac{\partial T}{\partial r}$$

In relation (1.34) at the melt–solid interface, derivatives and the front motion velocity normally to the curve $S_1(x, r)$ should be introduced. The conditions of the numerical experiment are chosen so that the plate thickness during irradiation decreases insignificantly due to vaporization. The most interesting melting-crystallization processes were observed, e.g., upon irradiation of a 0.27 mm-thick titanium plate. It was assumed that $\varepsilon = 0.25$, $r_f = 1$ mm, $q_0 = 1.5 \cdot 10^5$ W/cm^2, and $\tau = 7$ ms. Figure 1.11 presents the shapes of the melt pool after laser switching off. Because the melt surface temperature at the pool center by the pulse end exceeded the melting temperature by one and a half times, the melting boundary at the central region continued to move towards the plate bottom after laser switching off. At the same time, the peripheral region is cooled due to heat removal along the plate. The melt pool takes almost cylindrical shape. At later times, for $t > 30$ ms, surface thermal radiation losses begin to play a role. As a result, a liquid pool is produced inside the plate. The dynamics of crystallization fronts can determine the critical melting zone. Below, we will consider the two aspects of the vaporization process: the stability of a vaporization wave and the interaction of a vapor jet with the environment. The latter will be further used in the consideration of plasma phenomena near the surface.

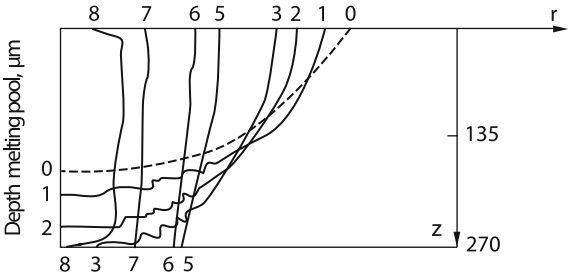

Fig. 1.11 Shape of a melt pool at different instants of time: (0) 7, (1) 8, (2) 10, (3) 12, (4) 14, (5) 20, (6) 25, (7) 35, (8) 40 ms

1.3.4 Stationary Interaction of a Vapor Jet with the Surrounding Gas

As was shown in the previous section, if $q \gg q_b$, the laser beam energy is completely spent to vaporize a material. The velocity of a vaporization wave propagating in the region of the material irradiated by the laser beam can be easily found from the mass expenditure $\dot{m} = \alpha q / L_b$ [see (1.31)]. Knowing the mass expenditure, it is easy to calculate the lowering rate v_e of the material level because the material density is known. As for the velocity of vapor, its determination is complicated because the density of the target vapor, depending on the pressure p_A of gas in which the target is located and the absorbed radiation intensity, is unknown. It is clear that for $q \geq q_b$, when $p_a \geq p_A$, vapor flies away from the target with a small subsonic velocity (p_a is the vapor pressure near the target). In this case, the vapor density near the target will be described by the expression $p_a \approx p_A$

$$\rho_a = p_A m / k_\mathrm{B} T_b \tag{1.41}$$

where m is the atomic mass of the target material. It is assumed in (1.41) that the gas temperature near the target surface is close to the boiling temperature T_b. Knowing ρ_a, we can determine from the law of conservation of mass and (1.31) the velocity v_1 near the target:

$$v_1 \approx \alpha q k_\mathrm{B} T_b / L_b p_A m \tag{1.42}$$

The values of ρ, v, and T change with distance from the target. We will discuss this question below, and now consider the behavior of the boundary values of gas-dynamic functions. According to (1.42), v_1 increases with increasing q and achieves the local sound speed $c_s(T_b)$ for $q = q_s$, where

$$\alpha q_s = L_b c_s p_A m / k_\mathrm{B} T_b \tag{1.43}$$

It is clear that as q is further increased, the gas velocity will no longer increase (for $T_s = T_b$) because the average velocity of atoms leaving the target surface cannot exceed the thermal velocity (see details in [30]). The law of conservation of mass flow for $q > q_s$ is satisfied due to the increase in the vapor density near the target:

$$\rho_a = \alpha q / L_b c_s \tag{1.44}$$

To find the surface temperature, it is necessary to recalculate the gas-dynamic values of v_1, ρ_a, and T_a to the corresponding values in the Knudsen layer on the target surface. For the supersonic flow, the recalculation expressions have the form [30]

$$T_a = 0.7 T_s \tag{1.45}$$

$$p_a = 0.2 p_s \tag{1.46}$$

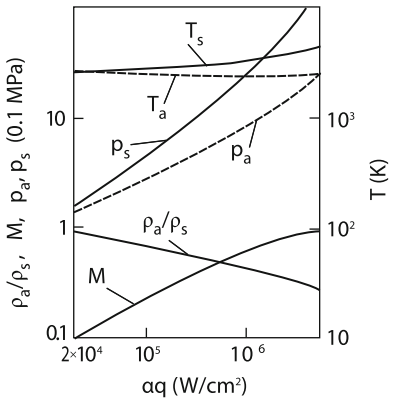

Fig. 1.12 Characteristics of the aluminum vaporization process in air

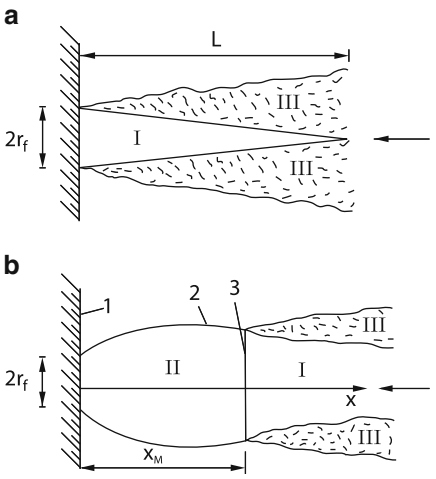

Fig. 1.13 Target vaporization process in air for subsonic (**a**) and supersonic (**b**) vapor flows; (1) target surface; (2) Barrel-shaped compression shock; (3) Mach disk; (I) Subsonic vapor flow region; (II) Supersonic vapor flow region; (III) Turbulent vapor flow region. The arrow shows the laser beam direction

where $p_s = p_0 \exp(-L_b/kT_s)$ is the saturated vapor pressure of the target material. In reality, the values of ρ, v and T_a change more smoothly with changing $q > q_b$. Figure 1.12 presents $p_a, \rho_a, T_a, p_s, \rho_s, T_s$ and the Mach number M for an aluminum target [31]. One can see that for $\alpha q = 4\,\mathrm{MW/cm^2}$, the flow near the target becomes supersonic. This value is well consistent with the value obtained for aluminum from expression (1.43). Thus, for $q < q_s$, the vapor flow is subsonic, while for $q > q_s$, it is supersonic.

Figure 1.13a shows the configuration of a subsonic flow [32, 33]. The estimate of the Reynolds number Re from the focal spot size gives the value 2,000–4,000, so that the subsonic jet flow is turbulent. It is known that the length L of a uniform central spot exceeds approximately by a factor of 9 the light spot radius r_f [34]. The thickness δ of the turbulent displacement region is determined by the turbulent kinematic viscosity v_T: $\delta \approx \sqrt{v_T x/v}$. In the turbulent region, where turbulent layers are merged, the velocity and temperature decrease proportionally to x^{-1}.

The configuration of the supersonic flow is shown in Fig. 1.13b [32, 33]. The main characteristic of such a flow is the position of the shock-wave front (the Mach disc)

$$x_M/d \approx 0.6(p_s/p_A)^{1/2} \tag{1.47}$$

The pressure behind the shock-wave front increases and then slowly decreases down to p_A. The density in the supersonic jet considerably decreases:

$$\rho = \frac{\rho_a}{2}\sqrt{\frac{\gamma-1}{\gamma+1}}\frac{d^2}{x^2},\ \gamma = c_p/c_v \tag{1.48}$$

while the velocity almost does not change:

$$v^2 = v_1^2(\gamma+1)/(\gamma-1)$$

Of interest is the value of density behind the shock-wave front, where the flow is subsonic:

$$\rho_d = \rho(\gamma+1)/(\gamma-1) = mp_A/0.7\gamma kT_s \tag{1.49}$$

One can see from (1.49) that the density behind the shock-wave front weakly differs from the density near the target in the case of the subsonic flow.

Note that the properties described above are confirmed experimentally with good accuracy upon laser irradiation of a target in a gas medium [35]. During irradiation of graphite target, the Mach disc was observed. It was shown experimentally that $x_M \sim (q/p_A)^{1/2}$, which also follows from theoretical expressions (1.44), (1.46), and (1.47).

1.4 Vaporization Kinetics and Hydrodynamics

Above, by considering qualitatively the vaporization of the metal surface exposed to laser radiation, we observed the variation of the vapor velocity near the target from zero up to the sound speed. The analysis was performed for vaporization to the atmosphere, i.e. in a medium with counterpressure. In the case of subsonic velocities, the gas-dynamic parameters were determined by the metal surface temperature, while in the case of the sound speed, the temperature and pressure jump was introduced (1.45) and (1.46). It is clear that this jump appears not only for supersonic flows. It should increase smoothly from zero in the absence of the flow (i.e. in the case of the equilibrium) up to its maximum value determined by (1.45) and (1.46). Generally speaking, the jump itself appears due to the description of the problem in the hydrodynamic approximation (see, e.g., review [36]). In reality, the parameters of the problem drastically change at a distance of the order of the mean free path of atoms in the Knudsen layer. This problem is analogous, for example, to the concept of a thermal jump near the solid–gas interface in a

strongly inhomogeneous temperature field (see, for example, [37]). The jump value in our case can be calculated similarly. We take into account that the velocity distribution function of vapor atoms flowing away from the metal surface is equal to the equilibrium Maxwell function at the metal surface temperature T_s:

$$f_M = n_s \left(\frac{m}{2\pi k T_s} \right)^{3/2} \exp\left(-\frac{mv^2}{2kT_s} \right), \; v_z > 0 \tag{1.50}$$

where $n_s = p_s / kT_s$ is the saturated vapor pressure. At a distance of the order of the mean free path from the surface, i.e. at the Knudsen layer boundary, the Maxwell velocity distribution function should be also established, but with the gas temperature T_a, density n_a, and hydrodynamic velocity u. The latter quantity is known only in the case of vaporization into vacuum or medium whose pressure is lower than the vapor pressure. Here, it is equal to the sound speed, i.e. the Mach number is $M = 1$. In other cases, the value of u is found by soling the gas-dynamic problem with boundary conditions n_a and T_a. Thus, the velocity distribution function at the Knudsen layer-gas interface has the form

$$f_r = n_a \left(\frac{m}{2\pi k T_a} \right)^{3/2} \exp\left\{ \left[-(v_z - u)^2 - v_r^2 \right] \Big/ \frac{2kT_a}{m} \right\} \tag{1.51}$$

It is reasonable to assume that a flow of particles incident on the metal surface is proportional to f_r [30, 38], i.e.

$$f_M = \beta_1 f_r, \; v_z < 0 \tag{1.52}$$

This assumption can be verified by solving a kinetic problem, which we will consider below. Then, it is necessary to satisfy the laws of conservation of particles, momentum and energy in the Knudsen layer. We obtain three equations for three unknowns n, T, and β. Figure 1.14 presents the results of numerical calculations of these equations depending on u or the Mach number. One can see that for $M = 1$, expressions (1.45) and (1.46) are obtained. This figure also presents the results obtained by other methods. Method 2 assumes the different velocity distribution function for atoms returning to the surface, which takes into account the influence of the parameters of a target on this function [39]. Model 3 assumes the dependence of this function only on the surface parameters T_s and n_s. All these functions are presented in Fig. 1.15. One can see that they most strongly differ from each other and numerical expression [40] in the region of small velocities. However, the moments of these functions, i.e. gas-dynamic parameters are close, which is well demonstrated in Fig. 1.14. Model 3 was used to study the dependence of the jumps of parameters in the Knudsen layer, when a part of atoms in vapor incident on the surface are reflected elastically or inelastically with the probability $1 - \alpha$ [48]. Here, α is the so-called accommodation coefficient. It is clear from general considerations that these atoms reduce the flow of atoms returning to the surface, thereby increasing jumps of n, T, and p on the Knudsen layer. This is especially

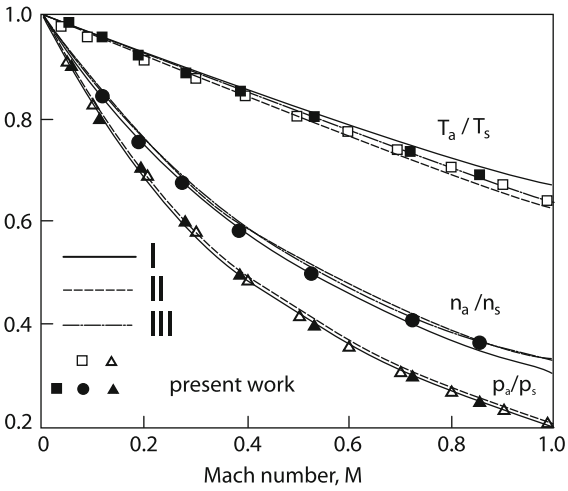

Fig. 1.14 Gas-dynamic boundary conditions for vaporization: the normalized temperature T_a, density n_a, and pressure p_a behind the Knudsen layer as functions if the Mach number M. Comparison of the numerical results of the presented model, the numerical results of Sone and Sugimoto [36], and analytic models I, II, and III (*curves*)

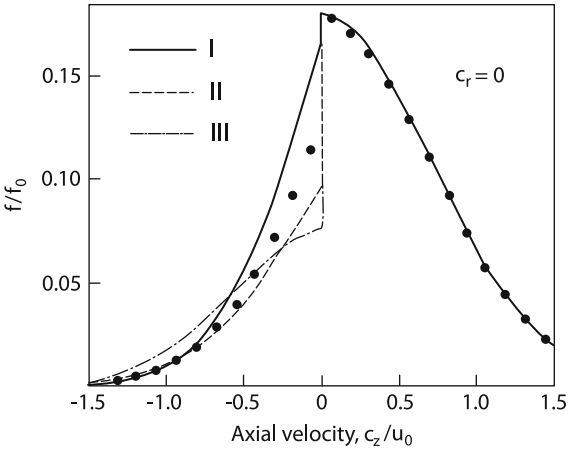

Fig. 1.15 Comparison of the numerical calculations of the velocity distribution function (*points*) and analytic models I, II, and III (*curves*) during vaporization for $p_a/p_s = 0.3$

pronounced for pressure Fig. 1.16. This figure also presents comparison with the case of diatomic vapor, which has a greater heat capacity than monatomic gas. One can see that the heat capacity weakly affects the pressure jump. A different situation is observed for the temperature jump Fig. 1.17. The jumps of the parameters are calculated based on the equality of flows. The expression for the equality of energy flows contains the heat capacities of vapors, and therefore the temperature jump will be smaller for vapor with the higher heat capacity. One can see from Fig. 1.16 that, as α decreases by half, pressures decreases approximately in the same way. Below, we will consider the inverse process of condensation and will show that the dependence of the jumps of parameters in the Knudsen layer on α is much stronger.

Thus, knowing the relation between the parameters of the gas and target at their interface, we can solve the problem of a sample heating in the case of developed vaporization. The propagation of heat in a solid in a moving coordinate

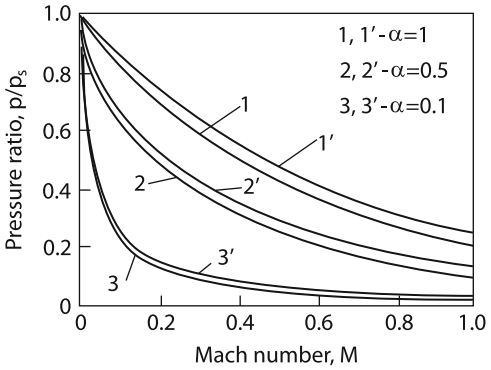

Fig. 1.16 Normalized pressure behind the Knudsen layer as a function of the Mach number for monoatomic (1, 2, 3) and polyatomic (1′, 2′, 3′) vapors

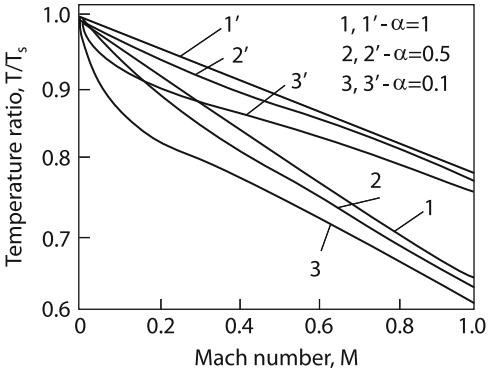

Fig. 1.17 Normalized temperature behind the Knudsen layer as a function of the Mach number for monoatomic (1, 2, 3) and polyatomic (1′, 2′, 3′) vapors

system coupled with the evaporating surface can be conveniently described for the enthalpy h

$$\frac{\partial h}{\partial t} + u_s \frac{\partial h}{\partial z} = \frac{\partial}{\partial z} \kappa \frac{\partial T}{\partial z} \tag{1.53}$$

where u_s is the velocity of the target-vapor interface, $u_s > 0$ if the target is evaporated and $u_s < 0$ if condensation proceeds. A change in the heat conductivity during melting is taken into account. The heat of melting can be taken into account by introducing enthalpy; if it is very small. then $h = c\rho T$. The continuity of the energy flow should be taken into account at the metal-gas interface. If the problem is considered within the framework of gas-dynamics, the relation

$$-\kappa \frac{\partial T_s}{\partial z} = q - E(n_a, T_a) \tag{1.54}$$

is used, where $E(n_a, T_a)$ is the heat flow carried away from the surface by vapor. Its value depends finally on n_s, T_s, and the Mach number M. In most of the problems of laser technology the absorbed power density q depends on time and coordinates. If vaporization occurs into vacuum or a medium with pressure that is considerably lower than the saturated vapor pressure at the target surface temperature, then

$M = 1$ and problem (1.53), (1.54) becomes closed and, correspondingly, solvable. However, here "underwater stones" can be encountered. It is necessary to be sure that the saturated vapor pressure at each moment exceeds the vapor pressure over the melt surface. As we saw above, this is a necessary requirement of the Anisimov–Knight model. For example, when the laser radiation intensity is drastically reduced, T_s will decrease so that this condition can be violated and condensation begins. Note that, if the decay time of the laser pulse intensity exceeds the unloading time due to the lateral expansion of vapor, we can assume that $M = 1$ when it is well known that the saturated vapor pressure exceeds the atmospheric pressure. This allows one to solve problem (1.53), (1.54) without the calculation of the dynamics of vapor. In this sense, two-dimensional problems can be simpler than one-dimensional ones, where the lateral unloading effect is absent.

It was pointed out above that relation (1.52) is generally speaking a priori. To substantiate it, a kinetic problem should be solved and compare the result with the gas-dynamic approach [42]. By solving the general problem of the action of a laser pulse on a target, it is necessary to find the energy flow leaving the surface at $z = 0$ [see (1.54)] by integrating the distribution function for $z = 0$:

$$E = \int v_z \left(H_b + \frac{mv^2}{2} \right) f \, \mathrm{d}\mathbf{V} \tag{1.55}$$

where H_b is the heat of vaporization of target atoms. To find the distribution function on the metal surface, it is necessary to solve the kinetic equation. Such kinetic problems are often solved by using the collision term in the simplified BGK (Bhatnagar–Gross–Krook) form [43]:

$$\frac{\partial f}{\partial t} + V_z \frac{\partial f}{\partial z} = \nu_0 (f_e - f) \tag{1.56}$$

where ν_0 is the relaxation frequency of the distribution function to the equilibrium function (1.51). The relaxation frequency in this model is found by equating heat conductions in the BGK model and the Chapmen–Enskog model of solid spheres [44]:

$$\nu_0 = \frac{32}{15} n d^2 \sqrt{\frac{\pi \kappa T}{m}} \tag{1.57}$$

As the boundary condition for (1.56) at $z = 0$, we use the semi-Maxwell distribution (1.50). Now the system of equations (1.50), (1.51), (1.55)–(1.57) is closed. The problem was solved numerically with the initial conditions $T(0) = 298\,\mathrm{K}$ and $f(0) = 0$. The calculation conditions were selected close to experimental conditions [45]. The laser pulse was bell-shaped, with the FWHM equal to 11 ns. Thermal parameters of a gold target are presented in Table 1.2. The results of calculations are presented in Fig. 1.18. One can see from Fig. 1.18a that the target surface temperature at the pulse trailing edge achieves the boiling point and then rapidly decreases down to the temperature at which vaporization ceases. Figure 1.18b

Table 1.2 Thermal parameters of gold

Heat capacity (solid)	28.8	J/(mol K)
Heat capacity (liquid)	31.3	J/(mol K)
Heat conduction (solid)	284	W/(m K)
Heat conduction (liquid)	155	W/(m K)
Melting temperature	1,336	K
Boiling temperature	3,150	K
Melting heat	12.6	kJ/mol
Boiling heat	331	kJ/mol
Atom diameter	0.236	nm

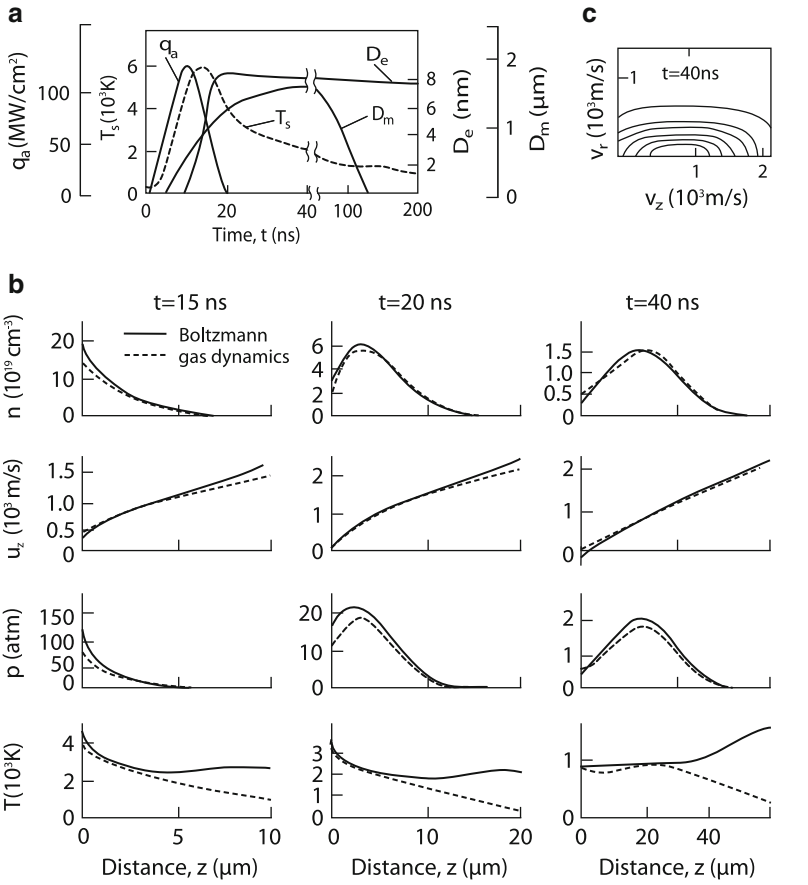

Fig. 1.18 The laser impulse form q_a, T_s is temperature of surface, D_e is evaporation depth, D_m is melt depth (**a**). The gas parameters vs z at different times (**b**). Velocity distribution function vs v_z and $v_r(c)$.

presents a comparison of the results of kinetic calculations with calculation of usual gas-dynamic equations with the Anisimov–Knight boundary conditions at the solid–gas interface. The difference between the results of these calculations, as expected, are observed at distances from the surface no more than 1 μm. For $t = 15$ ns, the

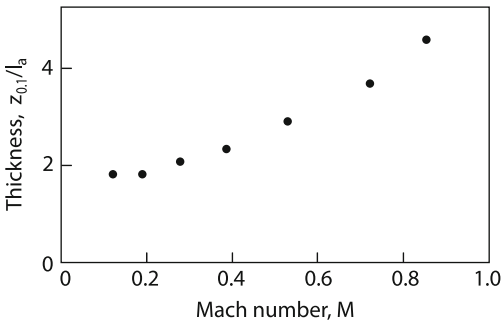

Fig. 1.19 Normalized thickness of the quasi-stationary Knudsen layer as a function of the Mach number during vaporization

mean free path l near the surface does not exceed 1 μm. Figure 1.19 presents the dependence of the Knudsen layer thickness on the Mach number. One can see that the Knudsen layer for the maximum value of M increases up to four mean free paths [40]. As expected, the strongest difference was observed between pressures, which also correspond to (1.46). At large distances $z > l$, where the hydrodynamic description can be applied, all parameters of a vapor cloud, calculated by different methods, coincide. In the cloud tail, at distances exceeding 5 μm, the mean free path becomes greater than the vapor cloud size. In this case, the kinetic and hydrodynamic approaches give substantially different results. As the vapor cloud expands in time, the region of coincidence of kinetic and hydrodynamic results also expands. It is interesting to observe the change in the velocity distribution of atoms with expanding the vapor cloud. This function is isotropic near the target (or at very low densities) and elongated in the expansion direction away from the target (Fig. 1.18c). These properties are important for PLD processes, which will be discussed in next chapters. Figure 1.18b demonstrates the limitation of the hydrodynamic model at $t = 40$ ns. One can see that the Anisimov–Knight condition is not fulfilled near the surface, and the density and pressure exceed their kinetic values. Condensation takes place, and the average velocity is negative. In this case, a comparison with experiment is also required because the kinetic equation is only a model one. Figure 1.20 compares the velocity and angular distributions of particles. Good agreement with experimental data is observed by selecting appropriately the laser pulse energy. The difference between distributions at large angles can be explained by the two-dimensional nature of vaporization in experiments due to a small focal spot.

1.4.1 Condensation

This process differs considerably from the vaporization process. In both processes, the relation between the saturated vapor and gas pressures is crucial. If $p_s/p_a > 1$, vaporization takes place, if $p_s/p_a < 1$, condensation occurs. However, as we saw, the gas temperature at the boundary during vaporization is a unique function of the

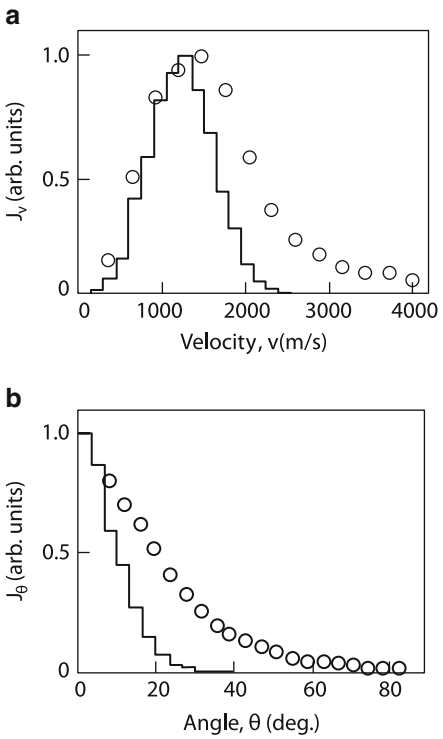

Fig. 1.20 Comparison of the calculated velocity $[J_v(v)]$ and angular $[J_\theta(\theta)]$ distributions of sputtered gold atoms (step lines) with experimental distributions (*points*) [45]: (**a**) velocity distributions averaged over the angular range from 5 to 29 degrees; (**b**) angular distribution averaged over the velocity range from 1,100 to 1,600 m/s. The calculated and experimental results are obtained for a 11 ns laser pulse. Other important parameters are following $E = 4.9\,\mathrm{J/cm^2}$ is the fluence of incident laser radiation; $E_\alpha = 1.5\,\mathrm{J/cm^2}$ is the absorbed laser fluence used in calculations; $t = 40\,\mathrm{ns}$ is the time at which the distributions were calculated

Mach number. Condensation can occur at different relations between the gas and surface temperatures $T_s > T_a$ and $T_s < T_a$. This is demonstrated in Figs. 1.21 and 1.22, where $T_a/T_s = 0.2$ and $T_a/T_s = 4$. In both cases, the Mach number increases with increasing pressure, i.e. condensation is accelerated. However, the passage to the sonic flow occurs at different p_s/p_a. This is well demonstrated in Fig. 1.22, where the gas pressure at which $M = 1$ increases by a fact or of three with increasing wall temperature. However, these pressure variations are negligible compared to temperature variations. These figures present the results of analytic models based on the same method as vaporization models [38, 39]. The models differ in the choice of the form of velocity distribution functions for vapor atoms flying to the sample surface. The analytic expression for the dependence of p_a/p_s on T_a/T_s obtained in one of the models is too cumbersome and is not presented here.

Note in conclusion that the diffuse reflection of atoms from the target surface considerably affects the boundary conditions of condensation [46]. This process is characterized by the condensation coefficient α. For $\alpha = 1$, all the atoms are thermalised on the target surface. For $\alpha \neq 1$, an addition proportional to $(\alpha - 1)$ is introduced into distribution function (1.50). Calculations show that these reflected atoms considerably reduce the condensation rate of vapor, Fig. 1.23. Figure 1.24

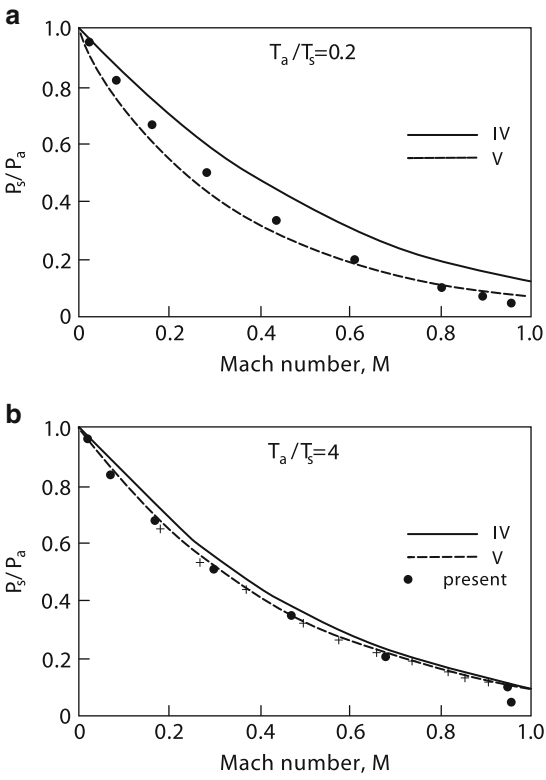

Fig. 1.21 Inverse pressure ratio p_a/p_s (**a**) as a function of the Mach number during condensation for $T_a/T_s = 0.2$ (**a**), $T_a/T_s = 4$ (**b**). *Circles* are numerical calculations; the *solid and dashed curves* correspond to models IV and V

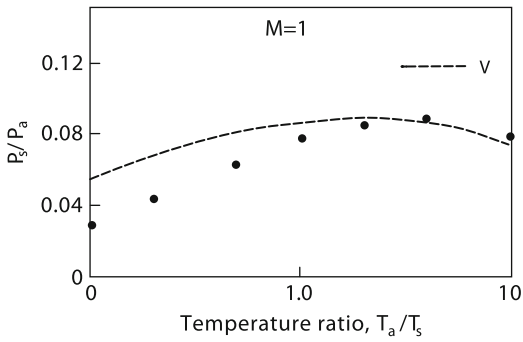

Fig. 1.22 Inverse pressure ratio p_a/p_s versus the temperature ratio T_a/T_s under sonic condensation (with $M = 1$): *points*, the numerical calculations; *broken curve*, Model V

[40] shows that the value of α determines the regions of temperature T_a/T_s where condensation can occur at the sound speed. Note that a small deviation of α from unity considerably affects the vapor condensation process. Thus, this circumstance should be also taken into account in the formulation of the pulsed ablation problem.

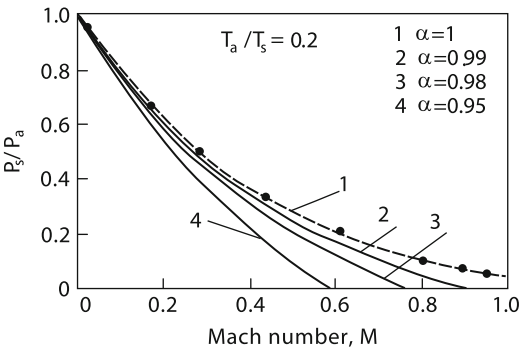

Fig. 1.23 Influence of the condensation coefficient on gas-dynamic conditions during condensation. The inverse vapor pressure ratio p_a/p_s as a function of the Mach number for $T_a/T_s = 0.2$ and different condensation coefficients. Circles are numerical values for $\alpha = 1$

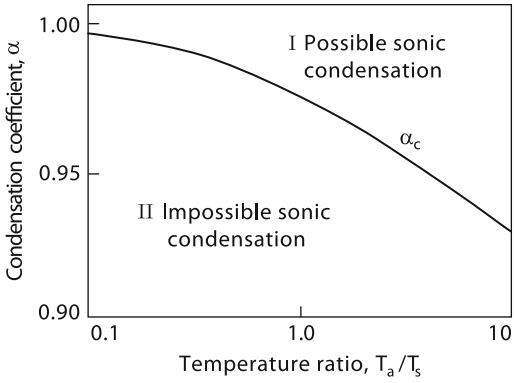

Fig. 1.24 The critical value of the condensation coefficient α_c as a function of T_a/T_s. Curve α_c divides two regions where sonic condensation is possible and impossible

1.5 Instability of the Laser-Induced Vaporization of Condensed Media

In the previous section, we considered effects taking place due to the nonequilibrium state of a condensed medium–vapor system. It is well known that in nonequilibrium media the instabilities often appear, resulting in the excitation of nonuniform oscillations with amplitude rapidly increasing in time. In this sense, the situation with the laser-induced vaporization of the condensed medium is very typical. Vaporization is an example of the first-order phase transition whose front is often unstable and has been long studied. Recall, for example, the formation of ice patterns during water freezing.

As for instability during vaporization, note that although this problem has been discussed in many papers (see, for example, [47] and references therein) the role of theoretically predicted instabilities in laser technology processes still remains unclear. This is explained by the fact that theories are restricted by the linear approximation when the oscillation amplitude is small. In addition, this problem is poorly studied experimentally.